

## ATMOSPHERIC HEAT REDISTRIBUTION ON HOT JUPITERS

DANIEL PEREZ-BECKER

Department of Physics, University of California, Berkeley, CA 94720, USA

AND

ADAM P. SHOWMAN

Department of Planetary Sciences, Lunar and Planetary Laboratory, University of Arizona, Tucson, AZ 85721, USA

*Draft version October 31, 2018*

### ABSTRACT

Infrared light curves of transiting hot Jupiters present a trend in which the atmospheres of the hottest planets are less efficient at redistributing the stellar energy absorbed on their daysides—and thus have a larger day-night temperature contrast—than colder planets. To this day, no predictive atmospheric model has been published that identifies which dynamical mechanisms determine the atmospheric heat redistribution efficiency on tidally locked exoplanets. Here we present a shallow water model of the atmospheric dynamics on synchronously rotating planets that explains why heat redistribution efficiency drops as stellar insolation rises. Our model shows that planets with weak friction and weak irradiation exhibit a banded zonal flow with minimal day-night temperature differences, while models with strong irradiation and/or strong friction exhibit a day-night flow pattern with order-unity fractional day-night temperature differences. To interpret the model, we develop a scaling theory which shows that the timescale for gravity waves to propagate horizontally over planetary scales,  $\tau_{\text{wave}}$ , plays a dominant role in controlling the transition from small to large temperature contrasts. This implies that heat redistribution is governed by a wave-like process, similar to the one responsible for the weak temperature gradients in the Earth’s tropics. When atmospheric drag can be neglected, the transition from small to large day-night temperature contrasts occurs when  $\tau_{\text{wave}} \sim \sqrt{\tau_{\text{rad}}/\Omega}$ , where  $\tau_{\text{rad}}$  is the radiative relaxation time and  $\Omega$  is the planetary rotation frequency. Alternatively, this transition criterion can be expressed as  $\tau_{\text{rad}} \sim \tau_{\text{vert}}$ , where  $\tau_{\text{vert}}$  is the timescale for a fluid parcel to move vertically over the difference in day-night thickness. These results subsume the more widely used timescale comparison for estimating heat redistribution efficiency between  $\tau_{\text{rad}}$  and the horizontal day-night advection timescale,  $\tau_{\text{adv}}$ . Only because  $\tau_{\text{adv}} \sim \tau_{\text{vert}}$  for hot Jupiters does the commonly assumed timescale comparison between  $\tau_{\text{rad}}$  and  $\tau_{\text{adv}}$  yield approximately correct predictions for the heat redistribution efficiency.

### 1. INTRODUCTION

Stellar radial velocity surveys have discovered a class of extrasolar planets whose masses are comparable to Jupiter’s, but that orbit their host stars at distances less than 0.1 AU (Lovis & Fischer 2010). In contrast to Jupiter, which roughly receives as much power from stellar irradiation as it releases from its interior, these “hot Jupiters” have power budgets dominated by external irradiation. In addition, the strong tidal torques are presumed to lock them into a state of synchronous rotation (Guillot et al. 1996), forcing them to have permanent daysides and nightsides. The extreme insolation, fixed day-night thermal forcing pattern, and slow rotation rates of hot Jupiters provide a unique laboratory to explore the atmospheric dynamics of giant planets under conditions not present in the Solar System.

Continuous photometric observations of eclipsing (transiting) hot Jupiters, over half an orbit or longer, allow for precise determination of the flux emitted from the planet as it presents different phases to us. Emission from the nightside is visible around the time the planet transits the stellar disk, while the dayside is visible just before and after the planet passes behind the star (secondary eclipse). The planetary contribution to the total flux received is up to  $\sim 0.1\%$ – $0.3\%$  at infrared wavelengths and can be isolated because the precise stellar flux is known from observations during secondary eclipse. The longitudinal atmospheric temperature profile of the planet is inferred from the orbital flux variations. These light curve observations are currently one of the most powerful tools to constrain the atmospheric dynamics of these planets (for a review, see Deming & Seager 2009). So far, visible and infrared light curves for at least 11 hot Jupiters have been published.

Figure 1 presents the fractional day-night flux differences, obtained from such light curves, for transiting hot Jupiters on near-circular orbits.<sup>1</sup> Specifically, we plot the flux difference between the dayside and nightside, divided by the dayside flux, as a function of the planet’s global-mean equilibrium temperature calculated assuming zero albedo. Interestingly, these light curve observations suggest an emerging trend wherein planets that receive greater stellar insolation—and therefore have hotter mean temperatures—exhibit greater fractional flux contrasts between the dayside and the nightside. Cool planets like HD 189733b (Knutson et al. 2007, 2009b, 2012) and HD 209458b (Cowan et al. 2007) have only modest day-night flux differences. Planets receiving intermediate flux, such as HD 149026b (Knutson et al. 2009a), exhibit intermediate day-night flux differences. And the most strongly irradiated planets, such as HAT-P-7b (Borucki et al. 2009), WASP-18b (Maxted et al. 2013), and WASP-12b (Cowan et al. 2012) exhibit fractional day-night flux differences close to unity.<sup>2</sup> This trend is consistent with a compar-

<sup>1</sup> In practice, we are dividing the amplitude of the phase curve variation by the depth of the secondary eclipse relative to the maximum in the phase curve, a procedure that only works for transiting hot Jupiters. Light curves of non-transiting hot Jupiters such as Ups And b (Harrington et al. 2006; Crossfield et al. 2010), 51 Peg b, and HD 179949b (Cowan et al. 2007) are therefore not included in Figure 1. We also exclude planets on highly eccentric orbits such as HD 80606b (Laughlin et al. 2009) and HAT-P-2b (Lewis et al. 2013).

<sup>2</sup> The HAT-P-7b point in Figure 1 lies in the visible, so there remains ambiguity about whether the dayside is bright due to thermal emission or due to reflected starlight. However, an unpublished full-orbit light curve of HAT-P-7b at  $3.6\mu\text{m}$  from Spitzer exhibits a phase-curve amplitude comparable to the secondary-eclipse depth (Knutson 2011), where emission is predominantly thermal rather than reflected starlight. This demonstrates that HAT-

ison of secondary eclipse depths with predicted dayside equilibrium temperatures in a broad sample of  $\sim 24$  systems performed by Cowan & Agol (2011). Together, Figure 1 and the analysis of Cowan & Agol (2011) suggest that the day-night temperature difference at the photosphere (expressed as a ratio to the dayside temperature) increases with effective temperature, and approaches unity for hot Jupiters with effective temperatures of  $\sim 2200$  K or greater.

What causes the trend observed in Figure 1? The commonly invoked explanation has been that the efficiency with which hot Jupiters redistribute heat is determined by the extent to which atmospheric winds transport hot gas across planetary scales faster than it takes the gas to radiate its heat into space. This balance is typically described by a comparison between two characteristic timescales, the timescale for winds to advect gas horizontally across the planet,  $\tau_{\text{adv}}$ , and the timescale for gas to reach local radiative equilibrium,  $\tau_{\text{rad}}$ . Showman & Guillot (2002) first suggested that hot Jupiters will exhibit large fractional day-night temperature differences when  $\tau_{\text{rad}} \ll \tau_{\text{adv}}$  and small fractional day-night temperature differences when  $\tau_{\text{rad}} \gg \tau_{\text{adv}}$ . They pointed out that the radiative time constant decreases strongly with increasing temperature, and they presented a heuristic theory suggesting that planets with greater characteristic radiative heating rates will exhibit larger fractional day-night temperature differences. Subsequently, a wide range of authors proposed that this timescale comparison could describe the pressure-, opacity-, and insolation-dependence of the day-night temperature differences on hot Jupiters (Cooper & Showman 2005; Showman et al. 2008; Fortney et al. 2008; Rauscher & Menou 2010; Heng et al. 2011; Cowan & Agol 2011; Perna et al. 2012). This picture is based on the expectation, from both three-dimensional (3D) circulation models and observations, that hot Jupiters should develop fast atmospheric jets capable of transporting heat over planetary scales.

However, this timescale comparison is neither self-consistent nor predictive, as  $\tau_{\text{adv}}$  is not known a priori and depends on many atmospheric parameters, including  $\tau_{\text{rad}}$ . In particular, one cannot even evaluate the criterion under given external forcing conditions unless one already has a theory for (or simulations of) the atmospheric flow itself. No such theory for the atmospheric circulation generally, or the day-night temperature difference specifically, has ever been presented. Moreover, the comparison between  $\tau_{\text{adv}}$  and  $\tau_{\text{rad}}$  neglects any role for other important timescales, including timescales for wave propagation, frictional drag, and planetary rotation. These timescales almost certainly influence the day-night temperature difference, among other aspects of the circulation. More generally, it is crucial to emphasize that the ultimate goal is not simply to obtain a timescale comparison for the transition between small and large day-night temperature difference, but rather to obtain a predictive theory for the day-night temperature difference itself, valid across the full parameter space.

To reiterate the role that other timescales can play, consider the Earth’s tropics. Over most of the tropics, the horizontal temperature gradients are weak, and the radiative cooling to space is balanced not by horizontal advection but by *vertical* advection (e.g., Sobel et al. 2001)—raising questions about the relevance of the horizontal advection time for this system.

P-7b indeed exhibits large fractional day-night temperature contrasts at the photosphere.

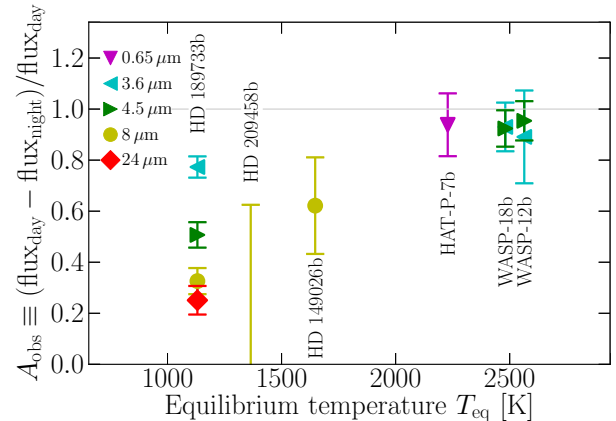


FIG. 1.— Fractional day-night infrared flux variations  $A_{\text{obs}}$  vs. global-mean equilibrium temperature  $T_{\text{eq}}$  for hot Jupiters with measured light curves. Here,  $A_{\text{obs}}$  is defined, at a particular wavelength, as the flux difference between dayside and nightside divided by the dayside flux. The equilibrium temperature is defined as  $T_{\text{eq}} = [F_*/(4\sigma)]^{1/4}$ , where  $F_*$  is the stellar flux received by the planet and  $\sigma$  is the Stefan-Boltzmann constant. Planets with hotter mean temperatures have larger day-night flux variations, indicating larger longitudinal temperature gradients at the photosphere. Colored symbols with error bars are from published observations (Knutson et al. 2007, 2009a,b, 2012; Cowan et al. 2007, 2012; Borucki et al. 2009; Maxted et al. 2013). The error bar without a data point for HD 209458b indicates that only an upper limit was published (Cowan et al. 2007).

In fact, the longitudinal variation of the temperature structure in the tropics is primarily regulated by adjustment due to gravity waves (see Showman et al. 2013b, for a review). Moist convection, gradients in radiative heating, and other processes can lead to horizontal temperature and pressure variations that in turn cause the generation of gravity waves. These waves induce horizontal convergence/divergence that, via mass continuity, causes air columns to stretch or contract vertically. This coherent vertical motion pushes isentropes up or down, and if the Coriolis force is weak (as it is in the tropics) and the waves are able to radiate to infinity, the final state is one with flat isentropes. A state with flat isentropes is a state with constant temperature on isobars; therefore, this wave-adjustment process acts to erase horizontal temperature differences. As emphasized by Bretherton & Smolarkiewicz (1989) and others, this adjustment process occurs on characteristic timescales comparable to the time for gravity waves to propagate over the length scale of interest. A key point is that, in many cases, this wave-propagation timescale is much shorter than the timescales for horizontal advection or mixing (e.g., between a cumulus cloud and the surrounding environment). Such wave propagation is not only local but can also occur over planetary scales, on both Earth (e.g., Matsuno 1966; Gill 1980; Bretherton & Sobel 2003) and exoplanets (Showman & Polvani 2011). Therefore, it is reasonable to expect that this wave-adjustment process will play a key role in the regulation of horizontal temperature differences on exoplanets—and, as a corollary, that the horizontal wave-propagation timescale will be important.

Motivated by these issues, our goals are to (1) quantify in numerical simulations how the day-night temperature difference on synchronously rotating exoplanets depends on external forcing parameters, (2) develop a quantitative theory for this behavior, and (3) isolate the dynamical mechanisms responsible for controlling the day-night temperature differences. A natural spin-off of this undertaking will be a cri-

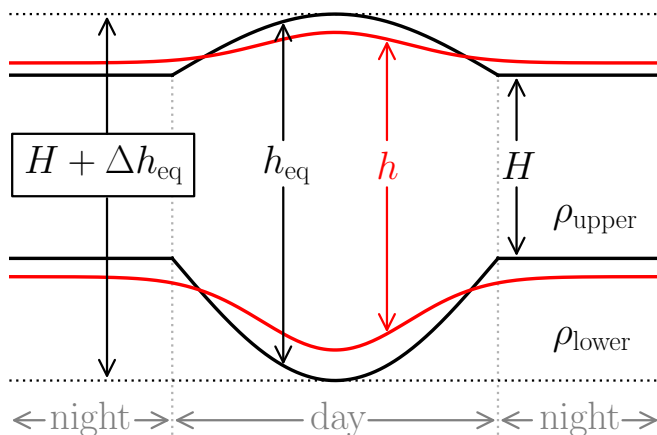


FIG. 2.— The two-layer shallow water model. A layer of fluid with constant density  $\rho_{\text{upper}}$  and variable thickness  $h$  floats above an infinitely deep layer of fluid with higher constant density  $\rho_{\text{lower}}$ . The fluid thickness  $h$  (red solid lines) represents the atmospheric mass column that has an entropy above a given reference value. Atmospheric heating thus will locally increase  $h$ , while cooling will locally reduce  $h$ . Radiative relaxation tends to restore the fluid to a temporally invariant profile,  $h_{\text{eq}}$  (black solid lines), over a radiative relaxation timescale  $\tau_{\text{rad}}$ . The radiative equilibrium profile, defined in equation (3), varies in height from  $H$  on the nightside to  $H + \Delta h_{\text{eq}}$  at the substellar point.

terion, expressed in terms of the various timescales, for the transition between small and large day-night temperature differences.

Because our emphasis is on developing a basic understanding, we adopt perhaps the simplest dynamical model that can capture the key physics: a shallow-water model representing the flow in the observable atmosphere. This means that our model will exclude many details important on hot Jupiters, but it will allow us to identify the key dynamical processes in the cleanest possible environment. We view this as a prerequisite to understanding more realistic systems.

Section 2 introduces our dynamical model. Section 3 presents numerical solutions of the atmospheric circulation and explores the dependence on external forcing parameters. Section 4 presents an analytic scaling theory of the day-night differences explaining the behavior of our numerical solutions. Section 5 provides a dynamical interpretation of the behavior in our theory and simulations. Section 6 applies this understanding to observations, and in particular we show that our model can explain the trend observed in Figure 1. Finally, Section 7 concludes.

## 2. THE MODEL

Global, 3D circulation models (GCMs) of planetary atmospheres involve many interacting processes, which makes it difficult to identify which dynamical mechanisms are dominating the solution. Simplified models have therefore played an important role in atmospheric dynamics of giant planets, both solar (Dowling & Ingersoll 1989; Cho & Polvani 1996; Scott & Polvani 2007; Showman 2007) and extrasolar (Cho et al. 2003, 2008; Showman & Polvani 2011; Showman et al. 2013a).

We study atmospheric heat transport on hot Jupiters with an idealized two-layer shallow-water model (see Figure 2). The buoyant upper layer of the model, having constant density  $\rho_{\text{upper}}$  and variable thickness  $h$ , represents the meteorologically active atmosphere of the planet. The infinitely deep bottom layer has a higher constant density  $\rho_{\text{lower}}$  and represents

the convective interior of the planet. We assume isostasy: the total mass column above a given depth in the lower layer is constant. For an infinitely deep lower layer, isostasy is guaranteed for baroclinic waves—those where the upper free surface and the interfacial boundary bow in opposite directions (Figure 2). Isostasy captures baroclinic modes but screens out barotropic ones (see Section 6.2 of Gill 1982); isostasy implies that there are no horizontal pressure gradients in the lower layer and therefore no horizontal velocities there. However, there can be vertical velocities; indeed mass will be transferred between the two layers.

The equations governing the upper layer are

$$\frac{d\mathbf{v}}{dt} + g\nabla h + f\mathbf{k} \times \mathbf{v} = \mathbf{R} - \frac{\mathbf{v}}{\tau_{\text{drag}}}, \quad (1)$$

$$\frac{\partial h}{\partial t} + \nabla \cdot (\mathbf{v}h) = \frac{h_{\text{eq}}(\lambda, \phi) - h}{\tau_{\text{rad}}} \equiv Q, \quad (2)$$

where  $\mathbf{v}(\lambda, \phi, t)$  is the horizontal velocity,  $h(\lambda, \phi, t)$  is the local thickness,  $t$  is time,  $g$  is the reduced gravity,<sup>3</sup>  $f = 2\Omega \sin \phi$  is the Coriolis parameter,  $\mathbf{k}$  is the vertical unit vector,  $\nabla$  is the horizontal gradient operator,  $\Omega$  is the planetary rotation frequency, and  $(\lambda, \phi)$  are the longitudinal and latitudinal angles. Here  $d/dt \equiv \partial/\partial t + \mathbf{v} \cdot \nabla$  is the time derivative following the flow (this includes curvature terms in spherical geometry).

Our equations apply to a two-layer system with a free upper surface. For a derivation, see equations (3.37) and (3.38) in Vallis (2006), which are identical to our equations with the exception of the source terms, which we explain below. Note that their momentum equation is written in terms of the height of the lower layer (their  $\eta_1$ ) above some reference level, whereas our equations are expressed in terms of the upper layer thickness ( $h$ ). Our momentum equation can be derived from theirs by noting that isostasy in the lower layer requires  $\nabla \eta_1 = -\nabla h \rho_{\text{upper}}/\rho_{\text{lower}}$ .

In local radiative equilibrium, the height field  $h(\lambda, \phi, t) = h_{\text{eq}}(\lambda, \phi)$ , with

$$h_{\text{eq}} = \begin{cases} H + \Delta h_{\text{eq}} \cos \lambda \cos \phi & \text{on the dayside} \\ H & \text{on the nightside,} \end{cases} \quad (3)$$

where  $H$  is the (flat) nightside thickness and  $\Delta h_{\text{eq}}$  is the difference in radiative-equilibrium thickness between the substellar point and the nightside (see Figure 2). The expression adopts a substellar point at  $(\lambda, \phi) = (0^\circ, 0^\circ)$ . The planet is assumed to be synchronously rotating so that  $h_{\text{eq}}(\lambda, \phi)$  remains stationary. Note that  $h_{\text{eq}}$  represents the two-dimensional height field set by local radiative equilibrium, whereas  $\Delta h_{\text{eq}}$  is its maximum deviation with respect to the layer thickness  $H$  at the nightside of the planet.

Equation (2) indicates that when the upper layer is not in radiative equilibrium, mass will be transferred between the layers, increasing or decreasing  $h$ . The relaxation toward equilibrium occurs over a radiative timescale  $\tau_{\text{rad}}$ —a free parameter

<sup>3</sup> The reduced gravity is the local gravitational acceleration times the fractional density difference between the upper and lower layers,  $g \equiv GM_{\text{planet}}/a^2 \times (\rho_{\text{lower}} - \rho_{\text{upper}})/\rho_{\text{lower}}$ , where  $G$  is the gravitational constant,  $M_{\text{planet}}$  is the planet mass, and  $a$  is the planet radius. Note that our definition of  $g$  differs from  $g'$  in Vallis (2006, see their Section 3.2), with  $g = g' \times \rho_{\text{lower}}/\rho_{\text{upper}}$ . The reduced gravity measures the restoring force at the interface between the two layers. When both layers have the same density, no pressure gradient forces exist and  $g = 0$ . Similarly, when  $\rho_{\text{upper}} \ll \rho_{\text{lower}}$ ,  $g$  will equal the full gravitational acceleration.

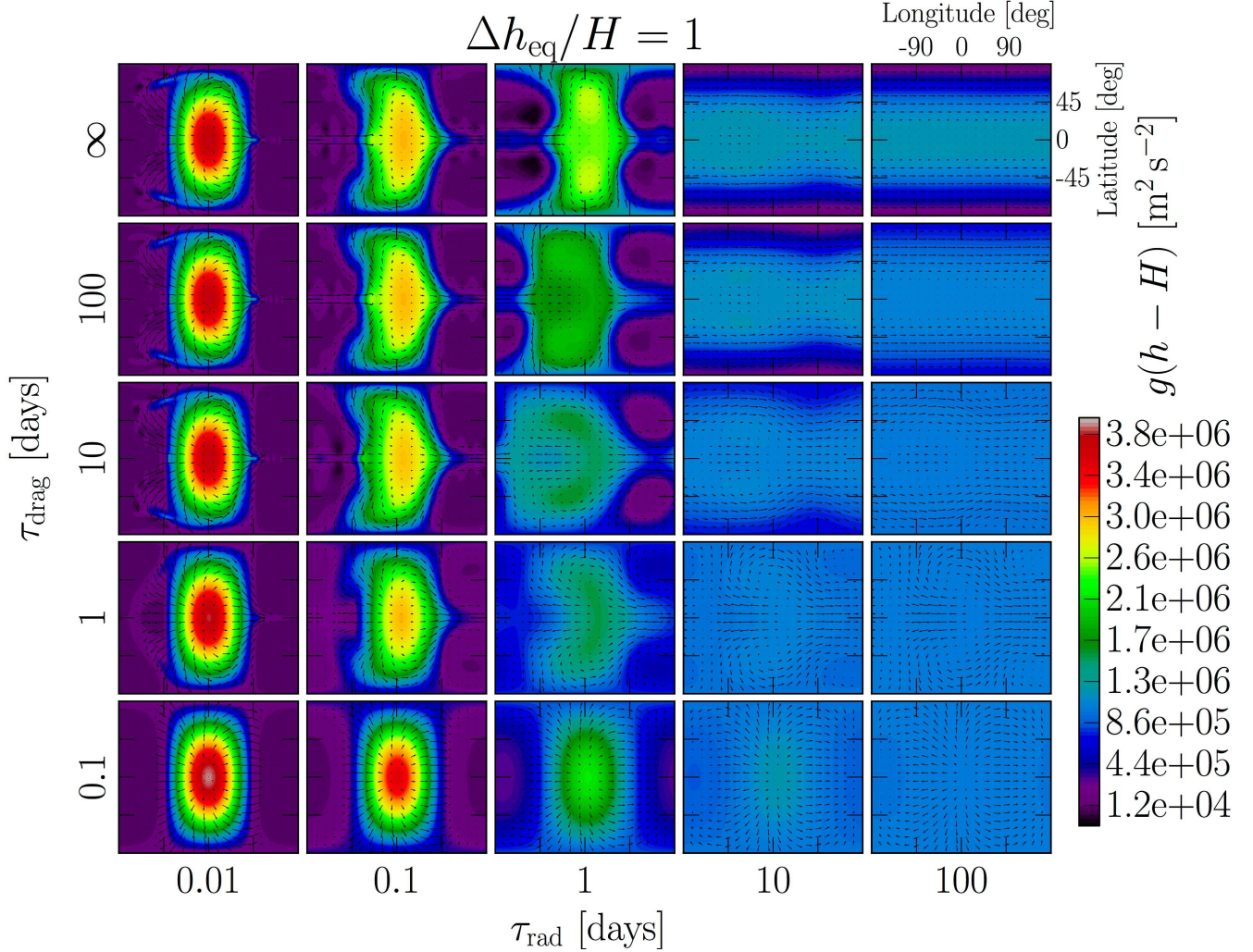


FIG. 3.— Equirectangular maps of steady-state geopotential ( $gh$ ) contours for the equilibrated solutions of the shallow-water model for a fractional forcing amplitude of  $\Delta h_{\text{eq}}/H = 1$ . We have subtracted the constant value of  $gH = 4 \times 10^6 \text{ m}^2 \text{ s}^{-2}$  from each panel. Overplotted are vector fields of the steady-state winds. Each panel in the grid was computed for a different combination of radiative and drag timescales,  $\tau_{\text{rad}}$  and  $\tau_{\text{drag}}$ , expressed in Earth days. Panels share the same scale for the geopotential, but wind speeds are normalized independently in each panel. The substellar point is located at the center of each panel, at a longitude and latitude of  $(0^\circ, 0^\circ)$ . Short radiative timescales result in steady-state  $gh$  profiles dominated by stellar forcing with a hot dayside and a cold nightside (see equation (3)), while the atmosphere relaxes to a constant  $gh$  for long values of  $\tau_{\text{rad}}$ . In contrast, the dependence of  $gh$  on  $\tau_{\text{drag}}$  is weaker. The atmospheric circulation shifts from a zonal jet pattern at long  $\tau_{\text{rad}}$  and  $\tau_{\text{drag}}$  to day-to-night flow when either  $\tau_{\text{rad}}$  or  $\tau_{\text{drag}}$  is reduced, as explained in detail in Showman et al. (2013a).

in the model. We can understand this mass transfer over a radiative timescale in the context of a 3D atmosphere. In a 3D context,  $h$  represents the amount of fluid having a specific entropy greater than a certain reference value—i.e.,  $h$  is a proxy for the mass column above an isentrope. In regions that are heated to return to local radiative equilibrium ( $Q > 0$ ), fluid acquires entropy and rises above the reference isentrope, increasing  $h$ . Likewise, in regions that cool ( $Q < 0$ ), fluid sinks below the reference isentrope, and  $h$  decreases.

Mass transfer between the horizontally static lower layer and the active upper layer will affect not only the local height of the upper layer but also its momentum. The momentum advected with mass transfer between layers is accounted for by  $\mathbf{R}$ —the vertical transport term. In regions where gas cools ( $Q < 0$ ), mass is locally transferred from the upper layer to the lower layer. This process should not affect the specific momentum of the upper layer, so  $\mathbf{R} = 0$  when  $Q < 0$ . In regions where gas is heated ( $Q > 0$ ) mass is transferred from the lower layer into the upper layer. The

addition of mass with no horizontal velocity to the upper layer should not affect its local column-integrated value of  $\mathbf{v}h$ . As explained by Showman & Polvani (2011), one can obtain an expression for  $\partial(\mathbf{v}h)/\partial t$  by adding  $\mathbf{v}$  times the continuity equation to  $h$  times the momentum conservation equation. When  $\partial(\mathbf{v}h)/\partial t = 0$ , terms involving heating and cooling ( $h\mathbf{R} + \mathbf{v}Q$ ) also have to vanish, which yields  $\mathbf{R} = -\mathbf{v}Q/h$  in regions of heating. This expression for  $\mathbf{R}$  is also used in Shell & Held (2004), Showman & Polvani (2010, 2011), and Showman et al. (2013a).

Finally, we parameterize atmospheric drag with Rayleigh friction,  $-\mathbf{v}/\tau_{\text{drag}}$ , where  $\tau_{\text{drag}}$  is a specified characteristic drag timescale. Potential sources of atmospheric drag are hydrodynamic shocks and Lorentz-force drag. The latter is caused by ion-neutral collisions induced by magnetic deflection of thermally ionized alkali metals. In this work we keep a general prescription for drag that is proportional to the flow velocity, at the cost of missing details of the individual physical processes (e.g., Lorentz-force drag only affects the flow

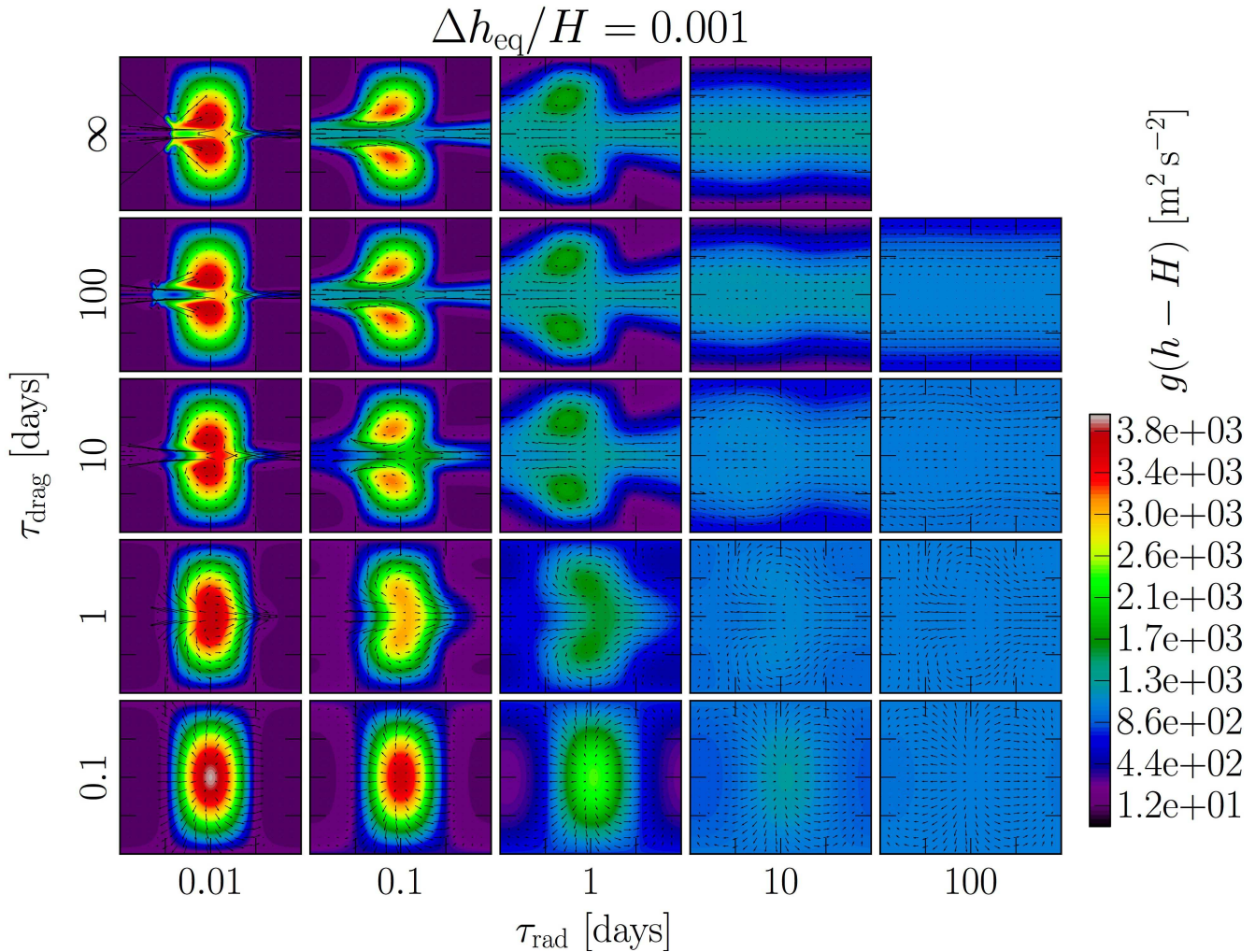


FIG. 4.— Same as Figure 3, but at a low forcing amplitude of  $\Delta h_{\text{eq}}/H = 0.001$ . Note that the dynamic range of the  $gh$ -contour color-scale has been reduced by a factor of 1000 compared to Figure 3. Wind speeds have also scaled down between figures. Comparing individual panels between Figures 3 and 4 reveals that even though the details of the solutions depend on  $\Delta h_{\text{eq}}/H$ , the characteristic value of the fractional day-night geopotential difference (normalized to the radiative equilibrium difference) remains largely unchanged.

component moving orthogonally to the local planetary magnetic field and strongly depends on the local gas temperature (Rauscher & Menou 2013)).

We solve equations (1) and (2) in global, spherical geometry with the following parameter choices. We choose  $g$  and  $H$  such that the gravity wave speed is  $\sqrt{gH} = (10 \text{ m s}^{-2} \times 400 \text{ km})^{1/2} = 2 \text{ km s}^{-1}$ .<sup>4</sup> For our fiducial hot Jupiter model,

<sup>4</sup> Our model is specified by the product  $gH$  and does not require separate specification of  $g$  and  $H$ , as can be seen by multiplying equation (2) by  $g$ . Gravity waves in our shallow water model are a proxy for internal gravity waves that exist in stratified atmospheres. In contrast to shallow water—where waves propagate exclusively in the plane perpendicular to gravity—gravity waves in a stratified atmosphere can propagate in any direction. Nevertheless, the latitudinal forcing on hot Jupiters will primarily excite horizontally traveling gravity waves whose propagation speeds will be similar to  $\sqrt{g_{\text{actual}} H_{\text{atm}}}$ , where  $g_{\text{actual}} \approx 10 \text{ m s}^{-2}$  is the full gravitational acceleration (not the reduced gravity) and  $H_{\text{atm}} \approx 400 \text{ km}$  is the atmospheric pressure scale height. Our nominal value for  $gH$  is chosen to match the propagation speed of the gravest mode of zonal gravity waves at the photosphere of hot Jupiters. Although it may be tempting to do so, we do not think of  $g$  as approximating  $g_{\text{actual}}$  (since the reduced gravity is conceptually distinct from and generally differs from the full gravity), nor do we think of  $H$  as approximating  $H_{\text{atm}}$ , since  $H$  is instead supposed to be a proxy for the thickness of material above an isentrope. Vertically propagating gravity waves are not captured by our model, but seem to be of lesser importance for the dynamics

we set the relative forcing amplitude  $\Delta h_{\text{eq}}/H = 1$ , implying that in radiative equilibrium temperature differences between day- and nightside vary by order unity. We will vary  $\Delta h_{\text{eq}}/H$  down to 0.001 to understand dynamical mechanisms and to verify that our theoretical predictions are valid in the linear forcing limit. Our values for the rotation frequency  $\Omega = 3.2 \times 10^{-5} \text{ s}^{-1}$  and a planetary radius of  $a = 8.2 \times 10^7 \text{ m}$  are similar to those of HD 189733b. The characteristic wave travel timescale is

$$\tau_{\text{wave}} \sim \frac{L}{\sqrt{gH}} \sim 0.3 \text{ Earth days}, \quad (4)$$

where  $L$  is the characteristic horizontal length scale of the flow. For typical hot Jupiters, this is comparable to  $L_{\text{eq}} \equiv (\sqrt{gH}a/2\Omega)^{1/2} \approx 5.1 \times 10^7 \text{ m}$ , the equatorial Rossby deformation radius—a natural length scale that results from the interaction of buoyancy forces and Coriolis forces in planetary atmospheres. Note that for a typical hot Jupiter,  $L$  and  $L_{\text{eq}}$  happen to be of the same order as the planetary radius  $a$  (Showman & Guillot 2002; Menou et al. 2003;

as they are not being excited by the longitudinal heating gradient—the driver of the system.

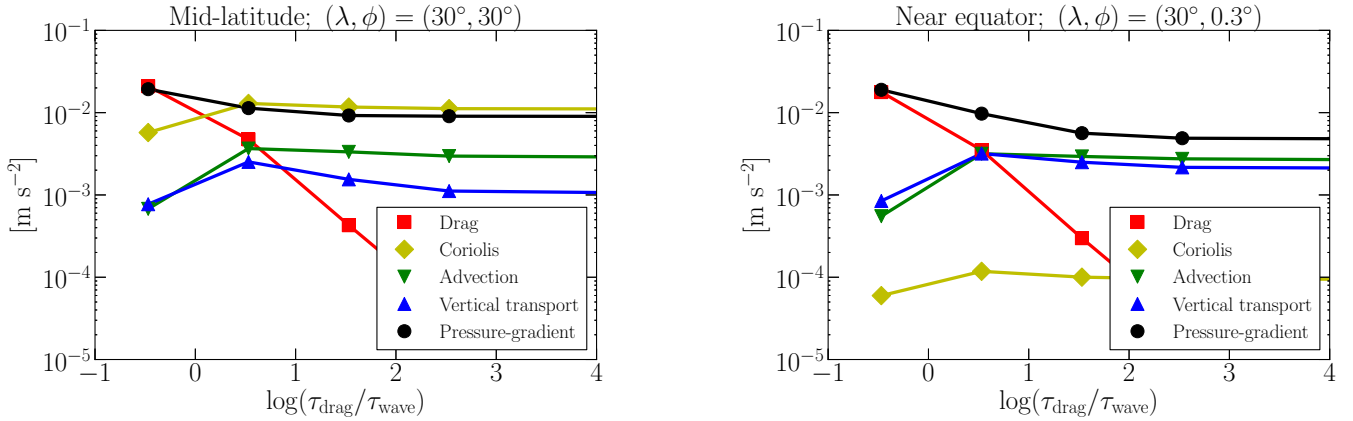


FIG. 5.— Absolute values of the zonal components of individual terms in the momentum equation (1) as a function of  $\tau_{\text{drag}}$ . For both panels,  $\Delta h_{\text{eq}}/H = 1$  and  $\tau_{\text{rad}}$  is held constant at 0.1 days [ $\log(\tau_{\text{rad}}/\tau_{\text{wave}}) = -0.5$ ]. The left panel is computed at a typical mid-latitude of the planet with coordinates  $(\lambda, \phi) = (30^\circ, 30^\circ)$ , while the right panel is computed near the equator  $(\lambda, \phi) = (30^\circ, 0.3^\circ)$ . Far away from the equator (left panel), the primary balance in the momentum equation is between the pressure-gradient force near either the Coriolis force (weak-drag regime) or drag (drag-dominated regime). The transition from the weak-drag regime to the drag-dominated regime in the momentum balance occurs when  $\tau_{\text{drag}} \sim 1/f$  (equation (19)). Near the equator (right panel) the primary term balancing the pressure-gradient force is either advection (together with the vertical transport term  $\mathbf{R}$ ) or drag.

Showman & Polvani 2011). We explore how the solution depends on the characteristic damping timescales  $\tau_{\text{rad}}$  and  $\tau_{\text{drag}}$ , which are free parameters in the model. In contrast, the characteristic time over which a gas parcel is advected over a global scale,  $\tau_{\text{adv}}$ , depends on the resulting wind profile and cannot be independently varied.

We solve equations (1) and (2) in spherical geometry with the Spectral Transform Shallow Water Model (STSWM) of Hack & Jakob (1992). The equations are integrated using a spectral truncation of T170, corresponding to a resolution of  $0.7^\circ$  in longitude and latitude (i.e., a  $512 \times 256$  grid in longitude and latitude). A  $\nabla^6$  hyperviscosity is applied to each of the dynamical variables to maintain numerical stability. The code adopts the leapfrog time-stepping scheme and applies an Asselin filter at each time step to suppress the computational mode. Models are integrated from an initially flat layer at rest until a steady state is reached. This system has been shown to be insensitive to initial conditions by Liu & Showman (2013). The models described here include those presented in Showman et al. (2013a), as well as additional models that we have performed for the present analysis.

In summary, the model contains three main input parameters:  $\tau_{\text{rad}}$ ,  $\tau_{\text{drag}}$ , and  $\Delta h_{\text{eq}}/H$ . Our main goal in Section 3 is to determine the dependence of the equilibrated fractional day-night height difference on these parameters. In Section 4 we develop a simple analytic scaling theory that reproduces trends found in the numerical model.

### 3. NUMERICAL SOLUTIONS

#### 3.1. Basic Behavior of the Solutions

As discussed in Section 1, observations indicate that as the stellar insolation increases, atmospheres transition from having small longitudinal temperature variations to having large day-night temperature contrasts. Our model solutions capture this transition, as shown in Figure 3. There, we plot the difference between the steady-state geopotential ( $gh$ ) and the nighttime geopotential at radiative equilibrium ( $gH$ ) for twenty-five models performed at high amplitude ( $\Delta h_{\text{eq}}/H = 1$ ) over a complete grid in  $\tau_{\text{rad}}$  and  $\tau_{\text{drag}}$ . Models are shown for all possible combinations of 0.01, 0.1, 1, 10, and 100 Earth days in  $\tau_{\text{rad}}$  and 0.1, 1, 10, 100, and  $\infty$  days in  $\tau_{\text{drag}}$ . In the context

of a 3D atmosphere,  $h$  represents the mass column above a reference isentrope; large  $h$  represents more material at high specific entropy (high temperature on an isobar). The stellar insolation is varied in the model by adjusting the damping timescales  $\tau_{\text{rad}}$  and  $\tau_{\text{drag}}$ . Generally, the higher the stellar flux (as measured by  $T_{\text{eq}}$ ), the lower  $\tau_{\text{rad}}$  will be. We will quantify the dependence of  $\tau_{\text{rad}}$  on  $T_{\text{eq}}$  in Section 6.

The models in Figure 3 capture major transitions in both the structure of the flow and the amplitude of the day-night thickness contrast. When  $\tau_{\text{rad}}$  is longer than one Earth-day, longitudinal gradients of  $gh$  are small. If  $\tau_{\text{drag}}$  is also long compared to a day, the circulation primarily consists of east-west-aligned (zonal) flows varying little in longitude (upper right corner of Figure 3). Despite the lack of longitudinal variation, such models exhibit an equator-pole gradient in  $gh$ , albeit with an amplitude that remains small compared to the radiative-equilibrium gradient. When  $\tau_{\text{rad}}$  is long but  $\tau_{\text{drag}}$  is short, winds flow from the dayside to the nightside over both the eastern and western hemispheres, and  $gh$  varies little in either longitude or latitude (lower right corner of Figure 3). Intermediate values of  $\tau_{\text{rad}}$  (e.g.,  $\sim 1$  day; middle column of Figure 3) lead to flows with greater day-night temperature differences and significant dynamical structure, including zonal-mean zonal winds that are eastward at the equator (i.e., equatorial superrotation). In contrast, when  $\tau_{\text{rad}}$  is short (left column of Figure 3), the geopotential amplitude and morphology closely match the radiative forcing profile: a spherical bulge on the hot dayside and a flat, cold nightside (see equation 3). The circulation consists of strong airflow from day to night along both terminators. Showman & Polvani (2011) and Showman et al. (2013a) showed that much of the wind behavior in Figure 3 (and in many published 3D global circulation models of hot Jupiters) can be understood in terms of the interaction of standing, planetary-scale waves with the mean flow.

Many of the characteristics of the full solution can be understood by studying the model under weak forcing ( $\Delta h_{\text{eq}}/H \ll 1$ ). In this limit, the day-night variations in  $h$  are much smaller than  $H$ , and terms in the shallow water equations exhibit their linear response. For example, the term  $\nabla \cdot (\mathbf{v}h)$  in the continuity equation will behave approximately as  $H\nabla \cdot \mathbf{v}$ . The

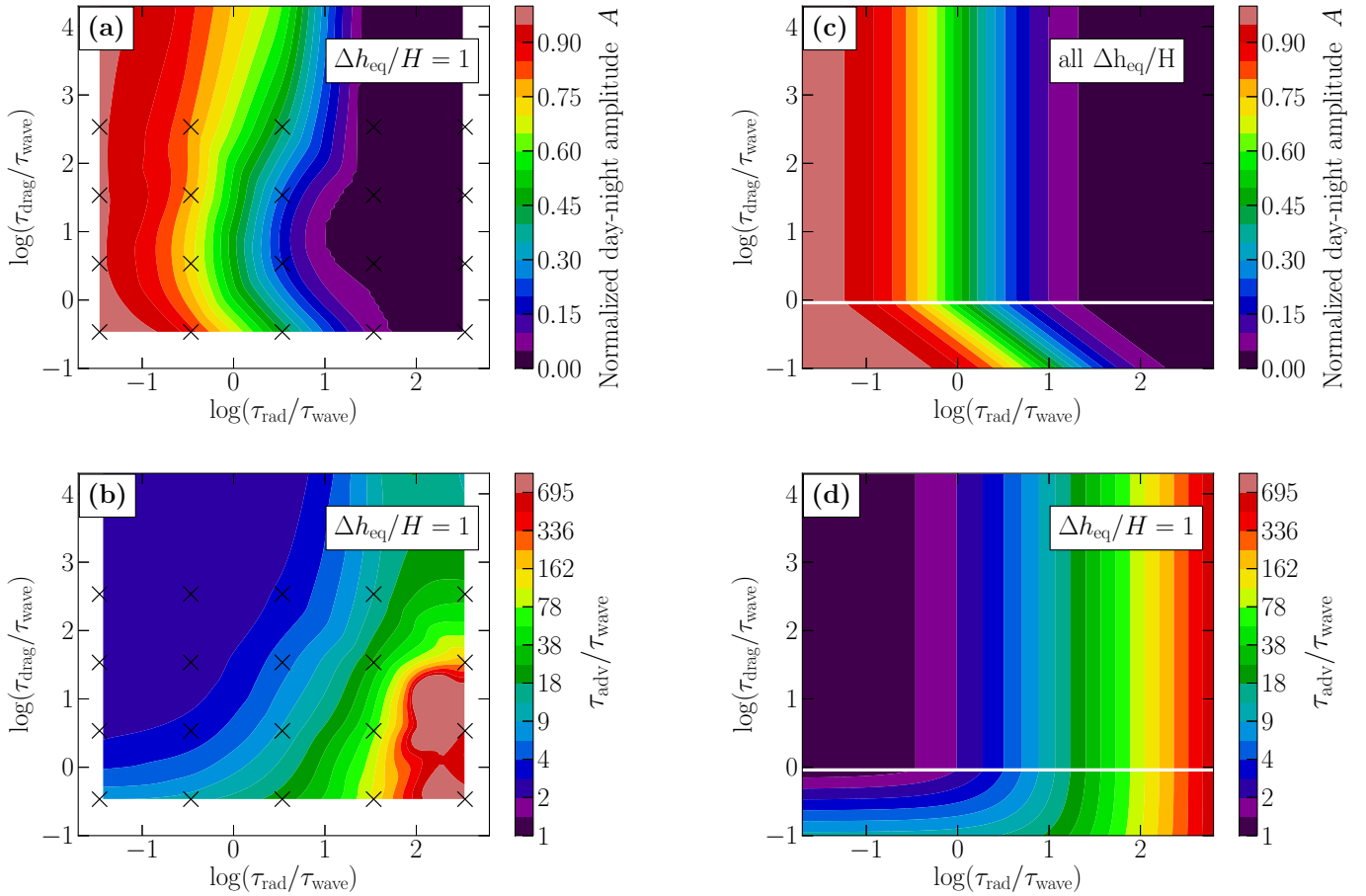


FIG. 6.— **Panel (a)**: contours of day-night height amplitude  $A$  (defined by equations (5)–(7)) as a function of  $\tau_{\text{rad}}$  and  $\tau_{\text{drag}}$  from our full numerical simulations with  $\Delta h_{\text{eq}}/H = 1$ . Values range from  $A = 0$ , which corresponds to a planet with a constant height field, to  $A = 1$ , which corresponds to a planet with  $h = h_{\text{eq}}$  everywhere, i.e., zero heat redistribution. Simulations were carried out for a matrix of  $\tau_{\text{rad}}$  and  $\tau_{\text{drag}}$  values as described in Figure 3. These runs are marked by the  $\times$  symbol; intervening values were calculated with a cubic-spline interpolation. In general terms, when  $\tau_{\text{rad}}$  is short compared to  $\tau_{\text{wave}}$ , atmospheres have a small heat redistribution efficiency. **Panel (b)**: contours of  $\tau_{\text{adv}}/\tau_{\text{wave}} \equiv \sqrt{gH}/U$  from these same simulations as a function of  $\tau_{\text{rad}}$  and  $\tau_{\text{drag}}$  with  $\Delta h_{\text{eq}}/H = 1$ . Here  $U$  is the RMS value of atmospheric winds (both zonal and meridional) averaged over the entire planet, and  $\sqrt{gH}$  is the gravity wave speed. Throughout the sampled space  $\tau_{\text{adv}}/\tau_{\text{wave}} > 1$ , with a minimum value of 2.1, colored purple. In the global mean, gravity waves always travel faster than winds. **Panel (c)**: contours of day-night geopotential amplitude  $A$  as a function of  $\tau_{\text{rad}}$  and  $\tau_{\text{drag}}$  as predicted by our analytical theory (equation (23)). Depending on the strength of atmospheric drag, different terms are being balanced in the momentum equation, yielding two distinct regions in the plot, separated by the solid white line, defined by equation (19). Drag is irrelevant in the upper region, but plays a significant role in the lower one. The simple timescale comparisons of our analytical theory broadly reproduce the results of the full numerical shallow-water model shown in panel (a). The scaling theory predicts that  $A$ -contours are independent of  $\Delta h_{\text{eq}}/H$ . **Panel (d)**: contours of  $\tau_{\text{adv}}/\tau_{\text{wave}}$  as a function of  $\tau_{\text{rad}}$  and  $\tau_{\text{drag}}$  as predicted by our analytical theory (equation (16) for the drag-dominated regime below the white line and equation (18) for the weak drag regime above the white line). In contrast to  $A$ , contour values of  $\tau_{\text{adv}}/\tau_{\text{wave}}$  depend on  $\Delta h_{\text{eq}}/H$ .

balance between  $H\nabla \cdot \mathbf{v}$  and  $Q$  in the continuity equation is linear. If the balance in the momentum equation is also linear, then wind speeds  $\mathbf{v}$  and amplitudes of  $h$ -variation should scale linearly with the forcing amplitude  $\Delta h_{\text{eq}}/H$ . In Figure 4 we present solutions of the model forced at the low amplitude of  $\Delta h_{\text{eq}}/H = 0.001$  for the same values for  $\tau_{\text{rad}}$  and  $\tau_{\text{drag}}$  as in Figure 3. Note that contour values for  $g(h - H)$  have been scaled down by a factor of 1000 from those in Figure 3. At this low amplitude, the system responds linearly for most of parameter space. A comparison of Figures 4 and 3 demonstrates that the low-amplitude behavior is extremely similar to the high-amplitude behavior when  $\tau_{\text{drag}}$  is short, but differs when  $\tau_{\text{drag}}$  is long. The amplitude dependence under weak-drag conditions is greatest when  $\tau_{\text{rad}}$  is short: at low amplitude, the mid-and-high latitudes are close to radiative equilibrium, whereas the equator exhibits almost no longitudinal variations in  $gh$ .

### 3.2. Physical Explanation for Forcing Amplitude Dependence

We now proceed to examine the reasons for these amplitude differences. Consider the principal force balances that determine the model solutions in the linear limit as a function of both drag and latitude.

For sufficiently strong drag ( $\tau_{\text{drag}} \lesssim 1$  day), the balance in the momentum equation is primarily between the pressure-gradient force—which drives the flow—and drag. This is a linear balance, and because the term balance in the continuity equation is likewise linear, we expect the  $h$ -field to scale with  $\Delta h_{\text{eq}}/H$ . This is indeed the case, as can be appreciated by the similarity of the lower panels of Figures 3 and 4.

When drag is reduced to the point where it becomes negligible ( $\tau_{\text{drag}} \gtrsim 1$  day), other terms in the momentum equation have to balance the pressure-gradient force. Which term plays the dominant role depends on the latitude of the planet. This is evident in Figure 4, where solutions in the upper left

corner have a flat  $h$ -field at the equatorial region, while the  $h$ -field has a day-night amplitude that approaches radiative equilibrium at high latitudes. For  $\Delta h_{\text{eq}}/H = 0.001$ , winds are weak, and away from the equator, the Rossby number  $Ro = U/fL \sim 0.001 \ll 1$ , where  $U$  is a characteristic horizontal wind speed. As a result, the primary force balance away from the equator is between the Coriolis force and the pressure-gradient force. This force balance is linear. Because the continuity equation is also linear, both  $h$  and  $\mathbf{v}$  should scale with  $\Delta h_{\text{eq}}/H$  at mid-latitudes. Comparing the upper rows of Figures 3 and 4 confirms that  $h$ -fields away from the equator scale with forcing amplitude in the weak-drag limit. Nevertheless, as the forcing amplitude is raised, wind speeds increase until  $Ro \sim 1$  when  $\Delta h_{\text{eq}}/H = 1$ . Therefore, the advective term becomes comparable to the Coriolis term at high amplitudes. This results in differences, but no fundamental changes, in the flow structure at high latitudes. The linear dynamics in the weak drag regime are described in more detail in Appendix C of Showman & Polvani (2011).

In the weak-drag limit, why does the equator exhibit large fractional height variations at large forcing amplitude but only small fractional height variations at small forcing amplitude? At the equator, the Coriolis force vanishes ( $Ro \gg 1$ ) and, if drag is weak, the force balance is between the pressure-gradient force and advection. This is an inherently non-linear balance because advection scales with the square of the velocity. Thus there is no linear limit for the dynamical behavior at the equator, and  $h$  will not scale linearly with  $\Delta h_{\text{eq}}/H$ . At  $\Delta h_{\text{eq}}/H = 1$ , the advection term is comparable to the Coriolis term at mid-latitudes. As a result, pressure (height) gradients remain as large at the equator as they are at mid-latitudes as can be appreciated in the upper rows of Figure 3. However, as the forcing amplitude is reduced to  $\Delta h_{\text{eq}}/H = 0.001$ , the advection term diminishes at a quadratic rate. To maintain balance with advection, the pressure-gradient force must also weaken as  $(\Delta h_{\text{eq}}/H)^2$ . Thus the height field becomes flat near the equator, as evidenced in the upper rows of Figure 4.

In Figure 5 we plot the magnitudes of the zonal components of all terms in the momentum equation as a function of  $\tau_{\text{drag}}$ . The term balances discussed above are apparent. Figure 5 is computed for  $\Delta h_{\text{eq}}/H = 1$ , with  $\tau_{\text{rad}}$  held constant at 0.1 days, while  $\tau_{\text{drag}}$  is varied in the abscissa. Note that Figure 5 normalizes  $\tau_{\text{drag}}$  with  $\tau_{\text{wave}}$ —the (constant) wave travel time (equation (4)). The relevance of  $\tau_{\text{wave}}$  will be explained in Section 4; from this point onward, we will express timescales in terms of  $\tau_{\text{wave}}$ . The left panel plots the terms at a typical mid-latitude with coordinates  $(\lambda, \phi) = (30^\circ, 30^\circ)$ , while the right panel is for a point near the equator  $(\lambda, \phi) = (30^\circ, 0^\circ)$ . As noted before, the pressure-gradient force away from the equator is balanced primarily against either the Coriolis force or drag. Near the equator, advection and vertical transport balance the pressure gradient when drag is weak.

### 3.3. Metric for the Day-Night Contrast

To compare our model solutions to the observed fractional flux variations of extrasolar planets, as well as to theoretical predictions, we need a measure similar to  $A_{\text{obs}}$  (see Figure 1). Our proxy for flux variations will be a day-night height difference  $A$  representative for the entire planet. We thus reduce each panel in Figures 3 and 4 to a single  $A$ , which we compute as follows. We start by evaluating the root-mean-square variations of  $h$  over circles of constant latitude, and normalize them to the values at radiative equilibrium:

$$A(\phi) = \left\{ \frac{\int_{-\pi}^{\pi} [h(\lambda, \phi) - \bar{h}(\phi)]^2 d\lambda}{\int_{-\pi}^{\pi} [h_{\text{eq}}(\lambda, \phi) - \bar{h}(\phi)]^2 d\lambda} \right\}^{1/2}, \quad (5)$$

where  $\bar{h}(\phi)$  is the zonally averaged height at a given latitude

$$\bar{h}(\phi) = \frac{1}{2\pi} \int_{-\pi}^{\pi} h(\lambda, \phi) d\lambda. \quad (6)$$

We then average  $A(\phi)$  over a  $60^\circ$  band centered at the equator

$$A = \frac{3}{\pi} \int_{-\pi/6}^{\pi/6} A(\phi) d\phi. \quad (7)$$

We find that for bands of width  $\gtrsim 60^\circ$ ,  $A$  becomes insensitive to the range in latitudes used for averaging. As defined,  $A$  can vary from 0, when  $h(\lambda, \phi, t) = \bar{h}(\phi)$  everywhere (corresponding to an atmosphere without longitudinal height variations), to 1, when the height equals that imposed by radiative forcing,  $h(\lambda, \phi, t) = h_{\text{eq}}(\lambda, \phi)$ .

Figure 6(a) shows how model values of  $A$  depend on the choice of damping timescales  $\tau_{\text{rad}}$  and  $\tau_{\text{drag}}$  (which have been normalized to  $\tau_{\text{wave}}$ ) for high-amplitude models with  $\Delta h_{\text{eq}}/H = 1$ . Models with short radiative time constants exhibit large fractional day-night differences. When the drag timescale is short ( $\tau_{\text{drag}}/\tau_{\text{wave}} < 1$ ), friction in the atmosphere starts to play a more important role in controlling the day-night height difference. Figure 6(b) shows contours of  $\tau_{\text{adv}}/\tau_{\text{wave}} \equiv \sqrt{gH}/U$  as a function of  $\tau_{\text{rad}}$  and  $\tau_{\text{drag}}$ . Here  $U$  is the RMS-value of atmospheric winds (both zonal and meridional) averaged over the entire planet, and  $\sqrt{gH}$  is the gravity wave speed. Throughout the sampled space  $\tau_{\text{adv}}/\tau_{\text{wave}} > 1$ , with a minimum value of 2.1, colored purple. Since  $\tau_{\text{wave}} < \tau_{\text{adv}}$  everywhere, the characteristic global-mean speed of gravity waves is always faster than the characteristic global-mean wind speed (however, note that, at the highest forcing amplitude, this is not always true locally everywhere over the globe).<sup>5</sup>

We can explain the qualitative behavior of these numerical solutions with an analytic theory in which we substitute dominant terms in the mass and momentum conservation equations with their order-of-magnitude counterparts. These analytical predictions, derived in Section 4, are showcased in Figures 6(c) and (d)—which are a reasonable match to Figures 6(a) and (b) showing the results of the numerical model. Two behaviors become apparent: above the white line of Figure 6(c), the contours are vertical, indicating that atmospheric drag does not affect the day-night temperature variation, a prediction that is in agreement with Figure 5. Below the white line, both the radiative and drag timescales affect  $A$ . Our scaling theory will confirm that  $\tau_{\text{wave}}$  plays a central role in controlling the heat redistribution efficiency.

<sup>5</sup> Supercritical flows with  $U > \sqrt{gH}$  occur near the day-night terminator in the long  $\tau_{\text{drag}}$  and short  $\tau_{\text{rad}}$  limit (upper-left panels in Figure 3). When supercritical flow rams into slower moving fluid, hydraulic jumps develop which convert some kinetic energy into heat (Johnson 1997). We do not account for this source of heating as it is likely to be modest and is only present for solutions where  $A$  is already  $\sim 1$ . Hydraulic jumps can also occur for supercritical flows in a stratified atmosphere. These are distinct from acoustic shocks that can develop in supersonic flow. The importance of acoustic shocks in modifying the photospheric temperature profile of hot Jupiters is still an open question, as most global simulations (including ours) do not capture the relevant physics, i.e., sound waves, and/or lack sufficient spatial resolution (Li & Goodman 2010).



In Figure 7 we show the variation of  $A$  (as defined in equations 5–7) with forcing amplitude  $\Delta h_{\text{eq}}/H$ . The morphology of  $A$  is largely independent of forcing strength. The two upper panels show the solution close to the linear limit, where we expect  $A$  to be independent of  $\Delta h_{\text{eq}}/H$ .<sup>6</sup> As  $\Delta h_{\text{eq}}/H \rightarrow 1$ ,  $Ro$  increases to order-unity values at mid-latitudes. Nevertheless, the Coriolis force remains comparable to or greater than advection in regions away from the equator (see the left panel of Figure 5). Thus, even for a large forcing amplitude,  $A$  remains largely independent of  $\Delta h_{\text{eq}}/H$ , because the primary force balance is close to linear. In contrast, the day-night difference evaluated solely at the equator,  $A_{\text{equator}} \equiv A(\phi = 0)$ , will depend on  $\Delta h_{\text{eq}}/H$ . In the left panels of Figure 8 we show  $A_{\text{equator}}$ -contours from our full numerical simulations as a function of  $\tau_{\text{rad}}$ ,  $\tau_{\text{drag}}$ , and  $\Delta h_{\text{eq}}/H$ . The right panels of Figure 8 show the  $A_{\text{equator}}$ -contours predicted by our scaling theory (Section 4). In the strong-drag regime (region below the white line), the behavior of  $A_{\text{equator}}$  in Figure 8 is relatively independent of amplitude, because the balance between drag and pressure-gradient forces is linear. In the weak-drag regime, the force balance is between advection and the pressure-gradient force. For this non-linear balance there is no linear limit for the dynamical behavior at the equator, and  $A_{\text{equator}}$  depends on the forcing amplitude.

#### 4. ANALYTIC THEORY FOR DAY-NIGHT DIFFERENCES

Here we obtain an approximate analytic theory for the day-night thickness differences and wind speeds in the equilibrated steady states. Our full numerical nonlinear solutions exhibit steady behavior, so the partial time derivatives in both the continuity and momentum equations can be neglected. The mass conservation equation (2) can thus be approximated as

$$h(\nabla \cdot \mathbf{v}) + \mathbf{v} \cdot \nabla h \sim \frac{h_{\text{eq}} - h}{\tau_{\text{rad}}}. \quad (8)$$

On the right side, the quantity  $h_{\text{eq}} - h$  gives the difference between the local radiative-equilibrium height field and the local height field (this difference is generally positive on the dayside and negative on the nightside). As shown in Figure 9,

$$|h_{\text{eq}} - h|_{\text{day}} + \Delta h + |h_{\text{eq}} - h|_{\text{night}} \sim \Delta h_{\text{eq}}, \quad (9)$$

where  $|h_{\text{eq}} - h|_{\text{day}}$  is the characteristic (scalar) difference between  $h_{\text{eq}}(\lambda, \phi)$  and  $h(\lambda, \phi, t)$  on the dayside and  $|h_{\text{eq}} - h|_{\text{night}}$  is the characteristic difference on the nightside. Define  $|h_{\text{eq}} - h|_{\text{global}}$  to be the arithmetic average between  $|h_{\text{eq}} - h|_{\text{day}}$  and  $|h_{\text{eq}} - h|_{\text{night}}$ .<sup>7</sup> Then, to order of magnitude,

$$|h_{\text{eq}} - h|_{\text{global}} \sim \Delta h_{\text{eq}} - \Delta h. \quad (10)$$

We thus can approximate  $h_{\text{eq}} - h$  in equation (8) with  $\Delta h_{\text{eq}} - \Delta h$ . The left side of equation (8) is, to order of magnitude,  $UH/L$ , where  $U$  is the characteristic horizontal wind speed and  $L$  is the characteristic horizontal lengthscale of the flow, which happens to be of order the planetary radius  $a$ .<sup>8</sup> Thus,

<sup>6</sup> For low  $\Delta h_{\text{eq}}/H$ , the non-linear equatorial region—defined by  $Ro \gtrsim 1$ —is thin and does not significantly contribute to the integral that makes up  $A$  in equation (7).

<sup>7</sup> The terms  $|h_{\text{eq}} - h|_{\text{day}}$  and  $|h_{\text{eq}} - h|_{\text{night}}$  are always of the same order because in steady state the rate at which mass is pumped into the active layer on the dayside ( $\propto |h_{\text{eq}} - h|_{\text{day}}/\tau_{\text{rad}}$ ) has to equal the rate at which mass is removed from the nightside ( $\propto |h_{\text{eq}} - h|_{\text{night}}/\tau_{\text{rad}}$ ).

<sup>8</sup> This scaling is actually subtle. Consider the first term on the left-hand side of equation (8). In a flow where the Rossby number  $Ro = U/fL \gtrsim 1$ , the divergence simply scales as  $\nabla \cdot \mathbf{v} \sim U/L$ . In a flow where  $Ro \ll 1$ , the flow is

we have for the continuity equation

$$H \frac{U}{L} \sim \frac{\Delta h_{\text{eq}} - \Delta h}{\tau_{\text{rad}}}. \quad (11)$$

The balance in the momentum equation (1) involves several possibilities. Generally, the pressure-gradient force  $-g\nabla h$ , which drives the flow, can be balanced by either atmospheric drag ( $-\mathbf{v}/\tau_{\text{drag}}$ ), the Coriolis force ( $-f\mathbf{k} \times \mathbf{v}$ ), horizontal advection ( $\mathbf{v} \cdot \nabla \mathbf{v}$ ), or the vertical transport term ( $\mathbf{R}$ ), which accounts for the momentum transfer from the lower layer. To order of magnitude, the balance is given by

$$g \frac{\Delta h}{a} \sim g \frac{\Delta h}{L} \sim \max \left[ \frac{U}{\tau_{\text{drag}}}, fU, \frac{U^2}{L}, \frac{U}{H} \frac{\Delta h_{\text{eq}} - \Delta h}{\tau_{\text{rad}}} \right]. \quad (12)$$

We solve equations (11) and (12) for the dependent variables  $\Delta h$  and  $U$ . In the following, we express  $\Delta h$  in terms of the dimensionless amplitude  $A$  (compare with equation 5):

$$A \sim \Delta h / \Delta h_{\text{eq}}. \quad (13)$$

We also non-dimensionalize  $U$  in terms of the timescale ratio  $\tau_{\text{adv}}/\tau_{\text{wave}}$ :

$$\tau_{\text{adv}}/\tau_{\text{wave}} \sim \sqrt{gH}/U. \quad (14)$$

There are four possible balances in equation (12). Which of the terms is balancing the pressure-gradient force will generally depend on the values of  $\tau_{\text{rad}}$ ,  $\tau_{\text{drag}}$ , the planetary latitude ( $\phi$ ), and the strength of forcing ( $\Delta h_{\text{eq}}/H$ ). Below we solve for the four possible term balances and describe the conditions under which they operate.

##### 4.1. Drag-dominated: Valid for Both Equatorial and Non-equatorial Regions

When drag is the dominant term balancing the pressure-gradient force, the solutions to equations (11) and (12) are

$$A \sim \left( 1 + \frac{\tau_{\text{rad}}\tau_{\text{drag}}}{\tau_{\text{wave}}^2} \right)^{-1}, \quad (15)$$

$$\frac{\tau_{\text{adv}}}{\tau_{\text{wave}}} \sim \left( \frac{\tau_{\text{drag}}}{\tau_{\text{wave}}} \right)^{-1} \left( \frac{\Delta h_{\text{eq}}}{H} \right)^{-1} \left( 1 + \frac{\tau_{\text{rad}}\tau_{\text{drag}}}{\tau_{\text{wave}}^2} \right). \quad (16)$$

Contours of equations (15) and (16) are shown in the region below the white horizontal line in Figures 6(c) and (d) ( $\tau_{\text{drag}} \lesssim \tau_{\text{wave}}$ ) and below the white curved line in the right panels of Figure 8. This white line marks the boundary of the drag-dominated regime in our model; we will formally define the white line transition in equation (19). The same expression for  $A$  as in equation (15) results when linearizing the full

geostrophically balanced; a geostrophically balanced flow has a horizontal divergence  $-\beta v/f$ , and there will be an additional possible ageostrophic contribution to the divergence up to order  $Ro U/L$ . Here,  $v$  is the meridional (north-south) wind velocity and  $\beta = df/dy$  is the gradient of the Coriolis parameter with northward distance  $y$ , equal to  $2\Omega \cos \phi/a$  on the sphere, where  $a$  is the planetary radius. Thus the geostrophic contribution to the horizontal divergence is  $v \cot \phi/a$ . Because the dominant flows on hot Jupiters have horizontal scales comparable to the Rossby deformation radius (Showman & Polvani 2011), which are comparable to the planetary radius for conditions appropriate to hot Jupiters, we have that  $L \sim a$ . Thus, the first term in Equation (8) scales as  $UH/L$  at a typical mid-latitude. Next consider the second term in Equation (8). When  $Ro \gtrsim 1$ , this term scales as  $U\Delta h/L$ . When  $Ro \ll 1$ , geostrophic balance implies that the geostrophic component of the flow is perpendicular to  $\nabla h$ , leaving only the ageostrophic component available to flow along pressure gradients. Thus, in this case, the second term scales as  $Ro U\Delta h/L$ . Because  $\Delta h \lesssim H$ , the first term generally dominates and the left-hand side of equation (8) therefore scales as  $UH/L$ .

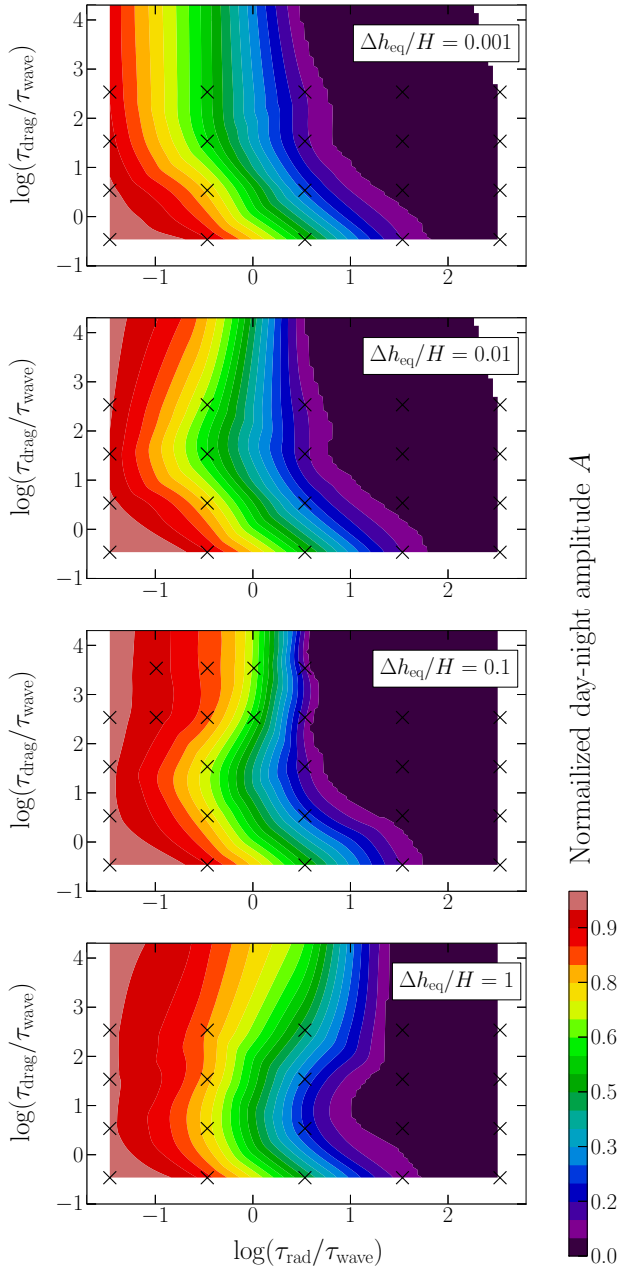


FIG. 7.— Contours of normalized day-night amplitude  $A$  (equations (5)–(7)) from our full shallow water simulations as a function of  $\tau_{\text{rad}}$  and  $\tau_{\text{drag}}$ . Each panel was computed for a different  $\Delta h_{\text{eq}}/H$ , ranging from 0.001 (top panel) to 1 (bottom panel). The lowermost panel is identical to Figure 6(a) and is repeated to facilitate a direct comparison with the other panels. Over the three orders of magnitude in  $\Delta h_{\text{eq}}/H$  shown, the morphology of  $A$  seems to remain roughly unchanged, with nearly vertical  $A$ -contours in the upper half of each panel and slanted  $A$ -contours for the lower half, where the drag force dominates the momentum equation. All panels compare well to our analytical scaling theory, shown in Figure 6(c).

model about a state of rest, where  $\tau_{\text{adv}} \rightarrow \infty$  (this linearization is carried out in detail in Showman & Polvani 2011).<sup>9</sup> This strongly suggests that in this region of the  $\tau_{\text{rad}}, \tau_{\text{drag}}$  plane, the

<sup>9</sup> To derive equation (15) from the shallow water equations, linearize a one-dimensional Cartesian version of equations (1) and (2), dropping the Coriolis term. Substitute one equation into the other to eliminate velocity. Impose sinusoidal forcing  $h_{\text{eq}} = \Delta h_{\text{eq}} \exp(ikx)$  and solve for steady, sinusoidal solutions of the form  $h = \Delta h \exp(ikx)$ . Finally, solve for  $A \sim \Delta h / \Delta h_{\text{eq}}$  to obtain the same expression as in equation (15).

advection timescale plays a minor role in controlling the day-night thickness and temperature differences. Indeed, Figure 6(d) shows that  $\tau_{\text{adv}}$  is always significantly larger than  $\tau_{\text{wave}}$  in this region. Equation (15) implies that the transition from small to large  $A$  occurs when  $\tau_{\text{wave}} \sim \sqrt{\tau_{\text{rad}} \tau_{\text{drag}}}$ . Note that the value of  $A$  in equation (15) is independent of the forcing strength  $\Delta h_{\text{eq}}/H$ . This is not true for the characteristic wind speed  $U$  and by extension  $\tau_{\text{adv}}$  (equation (16)).

#### 4.2. Coriolis-dominated: Valid for Non-equatorial Regions Only

When atmospheric drag is weak, the dominant balance in the force equation (12) depends on the Rossby number,  $Ro = U/fL$ . For conditions appropriate to hot Jupiters (typical rotation periods of a few Earth days, length scales comparable to a planetary radius, and wind speeds on the order of the wave speed or less), the Rossby number  $Ro \lesssim 1$ —except near their equators. For small  $Ro$ , the Coriolis force tends to dominate over horizontal advection and vertical transport (the last two terms in equation 12). Thus, away from the equator, we can balance the pressure-gradient force against the Coriolis force. In this case, equations (11) and (12) yield

$$A \sim \left(1 + \frac{\tau_{\text{rad}}}{f\tau_{\text{wave}}^2}\right)^{-1}, \quad (17)$$

$$\frac{\tau_{\text{adv}}}{\tau_{\text{wave}}} \sim \left(\frac{\Delta h_{\text{eq}}}{H}\right)^{-1} \left(f\tau_{\text{wave}} + \frac{\tau_{\text{rad}}}{\tau_{\text{wave}}}\right). \quad (18)$$

Contours of equations (17) and (18) are shown in the region above the white line in Figures 6(c) and (d), with the Coriolis parameter  $f$  evaluated at a latitude of  $\phi = 45^\circ$ . Notice the similarity between equations (15) and (17), where the role of  $\tau_{\text{drag}}$  has been replaced by  $1/f$ . Away from the equator, the Coriolis parameter  $f \sim \Omega$ , and equation (17) implies that the transition between small and large  $A$  occurs when  $\tau_{\text{wave}} \sim \sqrt{\tau_{\text{rad}}/\Omega}$ . The transition between the Coriolis-dominated and the drag-dominated regimes occurs when equations (15) and (17) are equal, a condition which yields

$$\tau_{\text{drag}} \sim 1/f. \quad (19)$$

This condition formally defines the white line transition between the Coriolis-dominated and drag-dominated regimes in Figures 6(c) and (d).

We combine our expressions for  $A$  and  $\tau_{\text{adv}}/\tau_{\text{wave}}$  valid away from the equator (equations (15) & (17) and (16) & (18), together with boundary condition equation (19)) to create Figures 6(c) and (d). These analytical results (derived for  $Ro \lesssim 1$ ) are a good representation of the globally averaged numerical results shown in Figures 6(a) and (b)—even though the former applies only for non-equatorial regions whereas the latter averages over both non-equatorial and equatorial regions. Nonetheless, the comparison we make between Figures 6(a) and (b) and Figures 6(c) and (d) is fair because either the equatorial solution shows trends in  $A$  and  $\tau_{\text{adv}}/\tau_{\text{wave}}$  similar to those of the mid-latitudes, or the equatorial region is small compared to the non-equatorial region (see Section 4.3).

Our analytical theory predicts that  $A$  is independent of the forcing strength ( $\Delta h_{\text{eq}}/H$ ) for the entire  $\tau_{\text{rad}}, \tau_{\text{drag}}$  plane. We test this prediction by running our numerical model at smaller  $\Delta h_{\text{eq}}/H$ . We show these results in Figure 7—indeed all panels exhibit the same general features of Figure 6(a).

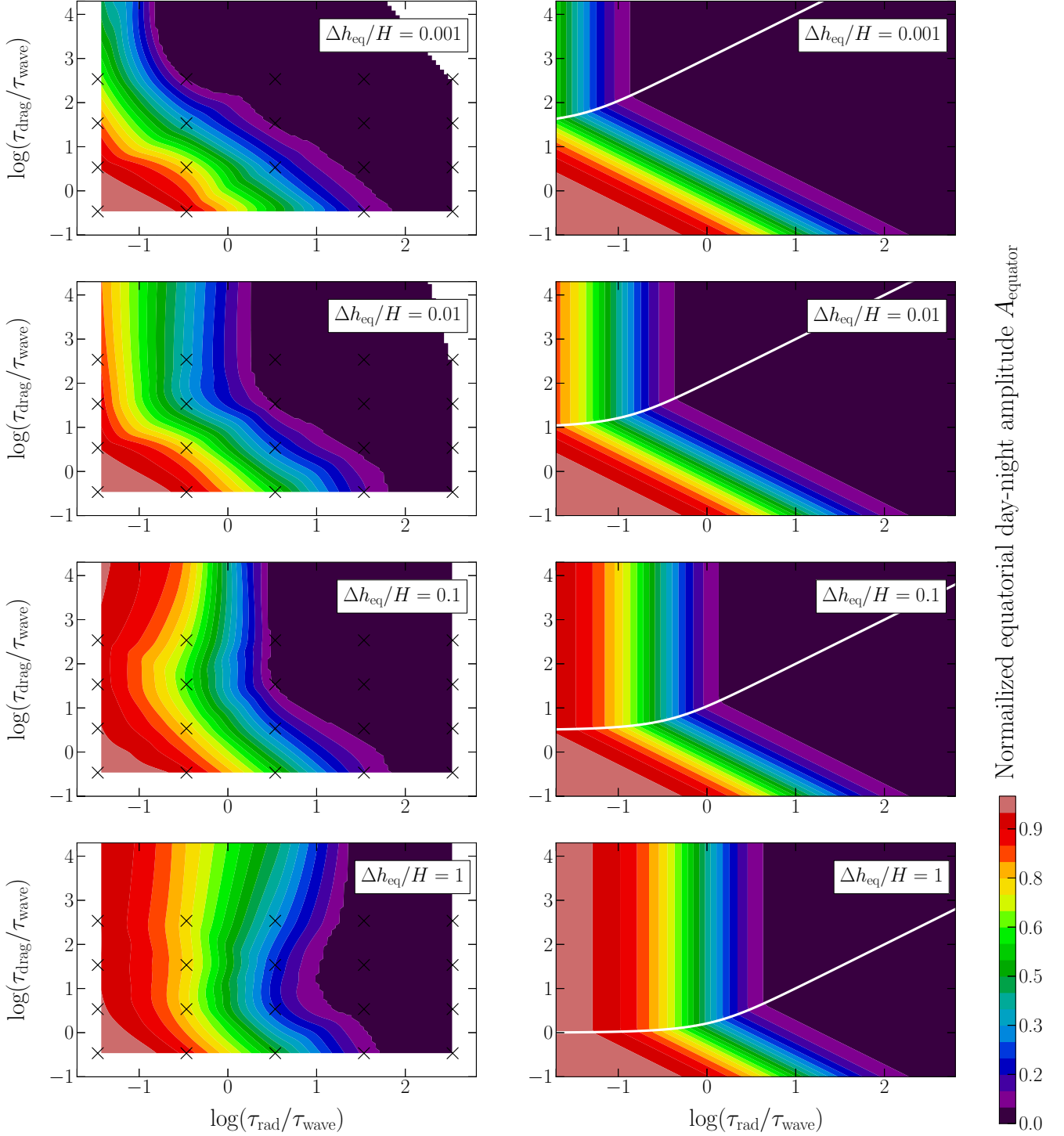


FIG. 8.— **Left-hand panels:** same as Figure 7, but for  $A_{\text{equator}}$ , the normalized day-night amplitude from our full shallow-water simulations evaluated only at the planetary equator. For  $\Delta h_{\text{eq}}/H = 1$ ,  $A_{\text{equator}}$  contours are similar to those of  $A$  (shown in the lowermost panel of Figure 7). But as  $\Delta h_{\text{eq}}/H$  is reduced, more of the  $\tau_{\text{rad}}$ ,  $\tau_{\text{drag}}$  parameter space becomes drag-dominated, characterized by slanted  $A_{\text{equator}}$  contours. At  $\Delta h_{\text{eq}}/H = 0.001$  (uppermost panel), most of the parameter space is drag dominated and the height field becomes flat at the equator when  $\tau_{\text{drag}} \rightarrow \infty$  (as can be appreciated directly from model solutions shown in the upper rows of Figure 4). **Right-hand panels:** normalized day-night equatorial amplitude  $A_{\text{equator}}$  as predicted from our scaling theory. The white line marks the transition from the low-drag regime (where  $A_{\text{equator}}$  is given by equation (20)) to the drag-dominated regime (where  $A_{\text{equator}}$  is given by equation (15)). Our theory compares well with the numerical shallow water solutions shown in the left panels of this figure.

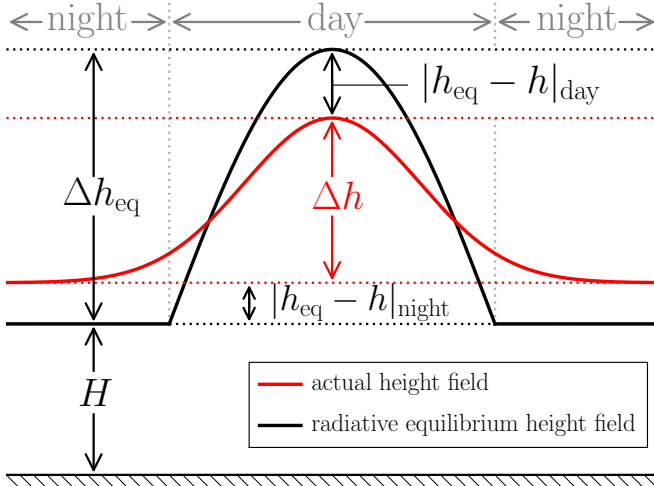


FIG. 9.— Simplified diagram of the upper layer of the shallow water model. We show this diagram as an aid to understanding equation (9). The interface between the upper and lower model layers is drawn as a flat floor (cf. Figure 2). Both the actual height field  $h$  (red solid line) and the radiative equilibrium height field  $h_{\text{eq}}$  (black solid line) are now measured with respect to this floor. We define a characteristic difference between  $h_{\text{eq}}$  and  $h$  on the dayside ( $|h_{\text{eq}} - h|_{\text{day}}$ ) and on the nightside ( $|h_{\text{eq}} - h|_{\text{night}}$ ) of the planet.

#### 4.3. Advection- or Vertical-transport-dominated: Valid for $Ro \gtrsim 1$

Near the equator (i.e.,  $Ro \gg 1$ ), the Coriolis force will vanish and the pressure-gradient force will be balanced by either advection or vertical transport. Both possibilities yield the same solution

$$A \sim 1 + \frac{1}{2} \left( \frac{\Delta h_{\text{eq}}}{H} \right)^{-1} \left( \frac{\tau_{\text{rad}}}{\tau_{\text{wave}}} \right)^2 \times \left\{ 1 - \left[ 1 + 4 \left( \frac{\Delta h_{\text{eq}}}{H} \right) \left( \frac{\tau_{\text{rad}}}{\tau_{\text{wave}}} \right)^{-2} \right]^{1/2} \right\}, \quad (20)$$

$$\frac{\tau_{\text{adv}}}{\tau_{\text{wave}}} \sim$$

$$\left[ \frac{\Delta h_{\text{eq}}}{H} + \frac{1}{2} \left( \frac{\tau_{\text{rad}}}{\tau_{\text{wave}}} \right)^2 - \sqrt{\frac{\Delta h_{\text{eq}}}{H} \left( \frac{\tau_{\text{rad}}}{\tau_{\text{wave}}} \right)^2 + \frac{1}{4} \left( \frac{\tau_{\text{rad}}}{\tau_{\text{wave}}} \right)^4} \right]^{-1/2} \quad (21)$$

We compare these analytical predictions for  $A$  at the equator (equations 15 and 20) with the equatorial day-night contrast of our numerical simulations—that is,  $A_{\text{equator}}$ —in Figure 8 (left panels are the numerical simulations, and right panels are analytical predictions). Notice how the weak drag solution (20) depends on forcing amplitude  $\Delta h_{\text{eq}}/H$ , whereas the strong drag solution (15) does not. The white line—marking the transition between the weak- and strong-drag regimes—is now a parabola, obtained by equating (15) and (20). As  $\Delta h_{\text{eq}}/H$  is reduced, wind speeds are reduced and a greater region of phase space is drag dominated.

For the strong forcing expected on hot Jupiters ( $\Delta h_{\text{eq}}/H \sim 1$ ), the numerical solution for the day-night contrast at the equator  $A_{\text{equator}}$  (lowermost panels in Figure 8) is very similar to the one obtained for mid-latitudes (Figures 6(a) and (c)), deviating by at most  $\sim 15\%$ . For weaker forcing, the solutions valid at mid-latitudes and the equator differ; however, at weak forcing, equations (20) and (21) are only valid in a narrow range of latitudes centered on the equator. This latitudinal range is delimited by the condition  $Ro = 1$  and can be

found analytically by solving

$$Ro = \frac{U}{fL} \sim 1 \sim \left( \frac{\sqrt{gH}}{2\Omega a} \right)^{1/2} \frac{1}{\sin \phi} \times \left[ \frac{\Delta h_{\text{eq}}}{H} + \frac{1}{2} \left( \frac{\tau_{\text{rad}}}{\tau_{\text{wave}}} \right)^2 - \sqrt{\frac{\Delta h_{\text{eq}}}{H} \left( \frac{\tau_{\text{rad}}}{\tau_{\text{wave}}} \right)^2 + \frac{1}{4} \left( \frac{\tau_{\text{rad}}}{\tau_{\text{wave}}} \right)^4} \right]^{1/2} \quad (22)$$

for  $\phi$ . For  $\Delta h_{\text{eq}}/H = (1, 0.1, 0.01, 0.001)$  the width of the equatorial region is at most  $\phi \sim (\pm 30^\circ, \pm 10^\circ, \pm 3^\circ, \pm 1^\circ)$  and goes to zero in the limit that the forcing amplitude goes to zero.

## 5. INTERPRETATION OF THEORY

### 5.1. Timescale Comparison

To give an executive summary of Section 4: we can reproduce the characteristic day-night difference  $A(\tau_{\text{rad}}, \tau_{\text{drag}}, \Delta h_{\text{eq}}/H)$  with a set of simple scaling relations

$$A \sim \begin{cases} \left( 1 + \frac{\tau_{\text{rad}} \tau_{\text{drag}}}{\tau_{\text{wave}}^2} \right)^{-1} & \text{when } \tau_{\text{drag}} \lesssim \Omega^{-1} \\ \left( 1 + \frac{\tau_{\text{rad}}}{\Omega \tau_{\text{wave}}} \right)^{-1} & \text{when } \tau_{\text{drag}} \gtrsim \Omega^{-1}, \end{cases} \quad (23)$$

which are valid for all forcing strengths ( $\Delta h_{\text{eq}}/H$ ) and nearly all latitudes (except those closest to the equator where  $A$  is given by equation (20) in the weak drag limit). We have found both numerically and analytically that a transition from a planet with uniform atmospheric temperature ( $A \sim 0$ ) to one with a large day-night temperature contrast relative to radiative equilibrium ( $A \sim 1$ ) occurs when

$$\begin{cases} \tau_{\text{wave}} \sim \sqrt{\tau_{\text{rad}} \tau_{\text{drag}}} & \text{when } \tau_{\text{drag}} \lesssim \Omega^{-1} \\ \tau_{\text{wave}} \sim \sqrt{\tau_{\text{rad}}/\Omega} & \text{when } \tau_{\text{drag}} \gtrsim \Omega^{-1}. \end{cases} \quad (24)$$

Wave adjustment would thus seem to play a key role in controlling whether or not the thermal structure of the day-night contrast is close to radiative equilibrium. In contrast, horizontal advection and radiative damping are usually considered the dominant factors for heat redistribution. The comparison between  $\tau_{\text{adv}}$  and  $\tau_{\text{rad}}$  is intuitive and provides a reasonable estimate for the heat redistribution efficiency on hot Jupiters (e.g., Perna et al. 2012), which are strongly forced ( $\Delta h_{\text{eq}}/H \sim 1$ ). Nevertheless, the  $\tau_{\text{adv}}$  vs.  $\tau_{\text{rad}}$  comparison is a poor predictor for  $A$  in the more general case, where  $\Delta h_{\text{eq}}/H$  is not of order unity. We now show this explicitly.

In Figure 10 we show  $A$ -contours as would be predicted by the  $\tau_{\text{rad}}$  vs.  $\tau_{\text{adv}}$  timescale comparison:

$$A \sim \left( 1 + \frac{\tau_{\text{rad}}}{\tau_{\text{adv}}} \right)^{-1}. \quad (25)$$

We chose the functional form for  $A$  in equation (25) because it possesses the correct limiting values (including  $A = 1/2$  when  $\tau_{\text{rad}} = \tau_{\text{adv}}$ ) and allows for a direct comparison with our results. Note that  $\tau_{\text{adv}} \propto U^{-1}$  is not an input parameter in the model; it has to be estimated either from the numerical solution or by using our scaling solutions (equations (16), (18), or (21)). In Figure 10, we set  $U$  equal to the global RMS value of the wind speed in the numerical model. At large forcing amplitude ( $\Delta h_{\text{eq}}/H = 1$ , lowermost panel) the contours of  $A$  as predicted by equation (25) show some resemblance to the numerical shallow water solution shown in Figure 7 (lowermost panel). Nevertheless, as the forcing amplitude is reduced, the

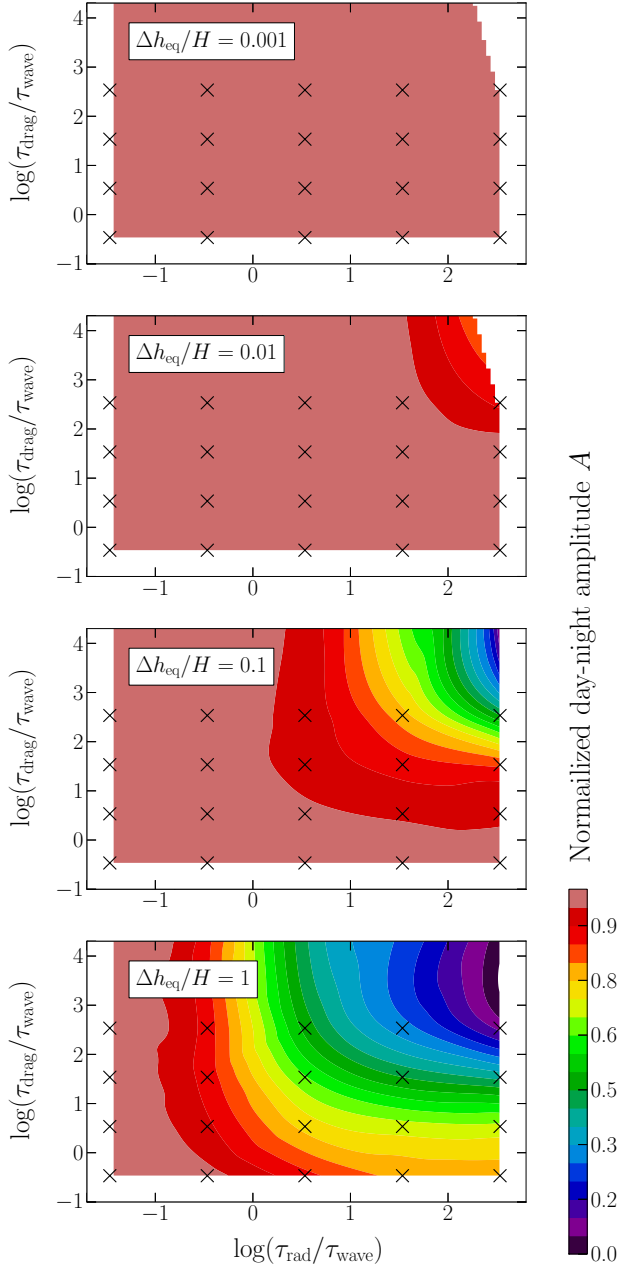


FIG. 10.— Contours of day-night height amplitude  $A$  as would be predicted by comparing  $\tau_{\text{rad}}$  vs.  $\tau_{\text{adv}}$ —the horizontal advective timescale. Values for  $A$  were computed with equation (25), where  $\tau_{\text{adv}} \equiv L/U$ , and  $U$  set to the global RMS value of the wind speed in the shallow water model. At  $\Delta h_{\text{eq}}/H = 1$  (lowest panel), the advective term in the momentum equation is of the same order of magnitude as other terms. As a result, comparison between  $\tau_{\text{adv}}$  and  $\tau_{\text{rad}}$  yields  $A$ -contours that show some similarity to the numerical results (Figure 6(a)). But as  $\Delta h_{\text{eq}}/H$  is reduced, the advective term dies off faster than other terms, making advection less relevant (with the exception of a thin band around the equator). By the time  $\Delta h_{\text{eq}}/H = 0.001$ ,  $\tau_{\text{adv}}$  has become so large compared to  $\tau_{\text{rad}}$  that equation (25) predicts  $A \rightarrow 1$  over the entire parameter space, clearly contradicting numerical results. The low forcing amplitude cases demonstrate that the height field in the shallow water model is not being predominantly redistributed by planetary-scale horizontal advection.

values of  $A$  predicted by equation (25) become increasingly inaccurate. In the limit where  $\Delta h_{\text{eq}}/H \rightarrow 0$ , equation (25) predicts  $A \rightarrow 1$  everywhere, because the characteristic wind speed  $U \propto \Delta h_{\text{eq}}/H$  (see equations (16) and (18)). In contrast, our numerical results show that  $A$ -contours are largely

independent of  $\Delta h_{\text{eq}}/H$ .

Rather than invoking Equation (25), we can demonstrate the breakdown of the  $\tau_{\text{rad}}$ -vs- $\tau_{\text{adv}}$  prediction in the low-amplitude limit simply by considering the ratio of these two timescales. When  $\Delta h_{\text{eq}}/H = 0.001$ , values of  $\tau_{\text{adv}}/\tau_{\text{rad}}$  vary between 30 and  $3 \times 10^5$  over our explored parameter space. Therefore, a  $\tau_{\text{rad}}$ -vs- $\tau_{\text{adv}}$  comparison would predict that the day-night thickness contrast is always very close to radiative equilibrium over the entire explored parameter space. This is inconsistent with our numerical simulations (Figures 4 and 7, top panel), which clearly show a transition from models close to radiative equilibrium at short  $\tau_{\text{rad}}$  to models with much smaller thermal contrasts at long  $\tau_{\text{rad}}$ .

It is clear that, at least for low forcing amplitudes, the amplitude of the day-night thermal contrast (relative to radiative equilibrium) is not controlled by a comparison between  $\tau_{\text{rad}}$  and  $\tau_{\text{adv}}$ . We now give two physical interpretations of the theory.

### 5.2. Vertical Advection

The timescale comparison in equation (24) can be obtained by comparing a *vertical* advection timescale to the radiative timescale. Define the vertical advection time,  $\tau_{\text{vert}}$ , as the time for a fluid parcel to move vertically over a distance corresponding to the day-night thickness difference  $\Delta h$ . The vertical velocity, by mass continuity, is  $\sim H \nabla \cdot \mathbf{v}$  (where  $\nabla$  is the horizontal gradient operator and  $\mathbf{v}$  is the horizontal velocity). Then

$$\tau_{\text{vert}} \sim \frac{\Delta h}{H \nabla \cdot \mathbf{v}} \sim \frac{\Delta h L}{H U}. \quad (26)$$

In the strong drag regime, equation (12) becomes  $\Delta h/U \sim L/(g\tau_{\text{drag}})$ , which when substituted into equation (26) implies that

$$\tau_{\text{vert}} \sim \frac{L^2}{gH\tau_{\text{drag}}} \sim \frac{\tau_{\text{wave}}^2}{\tau_{\text{drag}}}. \quad (27)$$

If  $\tau_{\text{rad}}$  is of order  $\tau_{\text{vert}}$ , then

$$\tau_{\text{rad}} \sim \tau_{\text{vert}} \sim \frac{\tau_{\text{wave}}^2}{\tau_{\text{drag}}}, \quad (28)$$

which is precisely the same comparison in equation (24) derived in the strong drag limit. Thus, our solution approaches radiative equilibrium ( $\Delta h \rightarrow \Delta h_{\text{eq}}$ ) when  $\tau_{\text{vert}} \gg \tau_{\text{rad}}$ , i.e., when  $\tau_{\text{wave}} \gg \sqrt{\tau_{\text{rad}}\tau_{\text{drag}}}$ . In other words, the atmosphere is close to radiative equilibrium when the vertical advection time (over a distance  $\Delta h$ ) is long compared to the radiative time. Conversely, the behavior is in the limit of small thickness variations ( $\Delta h \ll \Delta h_{\text{eq}}$ ) when  $\tau_{\text{vert}} \ll \tau_{\text{rad}}$ , i.e., when  $\tau_{\text{wave}}^2 \ll \tau_{\text{rad}}\tau_{\text{drag}}$ . In other words, the day-night thickness difference is small (compared to radiative equilibrium) when the vertical advection time is short compared to the radiative time.

In the Coriolis-dominated regime, the role of  $\tau_{\text{drag}}$  is replaced by  $f^{-1} \sim \Omega^{-1}$ , as can readily be seen in equation (12). Setting  $\tau_{\text{rad}}$  equal to  $\tau_{\text{vert}}$  now yields

$$\tau_{\text{rad}} \sim \tau_{\text{vert}} \sim \Omega \tau_{\text{wave}}^2, \quad (29)$$

which is the same timescale comparison in equation (24) for the Coriolis-dominated regime.

In either case, the relationship between the vertical and hor-

horizontal advection times follows directly from equation (26):<sup>10</sup>

$$\tau_{\text{vert}} \sim \tau_{\text{adv}} \frac{\Delta h}{H}. \quad (30)$$

Therefore, the vertical advection time,  $\tau_{\text{vert}}$ , is smaller than the horizontal advection time by  $\Delta h/H$ . The vertical and horizontal advection times become comparable when day-night thickness differences are on the order of unity (which can occur only for large forcing amplitudes  $\Delta h_{\text{eq}}/H \sim 1$ ). Only in that special case, will a comparison between  $\tau_{\text{rad}}$  and the horizontal advection time,  $\tau_{\text{adv}}$ , give a roughly correct prediction for  $A$  (as previously mentioned in Section 5.1 and shown in the bottom panel of Figure 10).

The physical reason for the importance of  $\tau_{\text{vert}}$  over  $\tau_{\text{adv}}$  in controlling the transition stems from the relative roles of vertical and horizontal advection in the continuity equation (8). When  $\Delta h/H$  is small, the term  $h\nabla \cdot \mathbf{v}$ —which essentially represents vertical advection—dominates over the horizontal advection term  $\mathbf{v} \cdot \nabla h$  (see footnote 8). Thus, under conditions of small  $\Delta h/H$ , the dominant balance is between radiative heating/cooling and *vertical*, rather than horizontal, advection. This is precisely the shallow-water version of the so-called “weak temperature gradient” (WTG) regime that dominates in the Earth’s tropics, where the time-mean balance in the thermodynamic energy equation is between vertical advection and radiative cooling (Sobel et al. 2001; Bretherton & Sobel 2003). Only when  $\Delta h/H \sim 1$  does horizontal advection generally become comparable to vertical advection in the local balance.

### 5.3. Wave Adjustment Mechanism

As described in Section 1, gravity waves are known to play a central role in regulating the thermal structure in the Earth’s tropics (Bretherton & Smolarkiewicz 1989; Sobel 2002; Showman et al. 2013a). Likewise, our analytic scaling theory (Section 4) shows the emergence of a wave timescale in controlling the transition from small to large day-night temperature difference in our global, steady-state solutions. This is not accidental but strongly implies a role for wave-like processes in governing the dynamical behavior. Although our numerical simulations and theory stand on their own, we show here that they can be interpreted in terms of a wave adjustment mechanism.

To illustrate, consider a freely propagating gravity wave in the time-dependent shallow-water system. In such a wave, horizontal variations in the thickness ( $h$ ) cause pressure-gradient forces that induce horizontal convergence or divergence, which locally changes the height field and allows the wave structure to propagate laterally. In fact, it can easily be shown that this physical process—namely, vertical stretching/contraction of atmospheric columns in response to horizontal pressure-gradient forces—naturally leads to a wave timescale  $\tau_{\text{wave}} \sim L/\sqrt{gH}$  for a freely propagating wave to propagate over a distance  $L$ .<sup>11</sup> Now, although our solutions in Section 3 lack freely propagating waves (being forced,

damped, and steady), the key point is that the *same physical mechanism* that causes wave propagation in the free, time-dependent case regulates the day-night thickness variation in our steady, forced, damped models. In particular, in our hot-Jupiter models, the dayside mass source and nightside mass sink cause a thickening of the layer on the dayside and a thinning of it on the nightside; in response, the horizontal pressure-gradient forces cause a horizontal divergence on the dayside and convergence on the nightside, which attempts to thin the layer on the dayside and thicken it on the nightside. Although technically no phase propagation occurs in this steady case, this process—being essentially the same process that governs gravity-wave dynamics—nevertheless occurs on the gravity-wave timescale. This is the reason for the emergence of  $\tau_{\text{wave}}$  in our analytic solutions in Section 4.

The situation on a rotating planet is more complex, because the Coriolis force significantly modifies the wave behavior. On a rotating planet, freely propagating, global-scale waves within a deformation radius of the equator split into a variety of equatorially trapped wave modes, including the Kelvin wave and equatorially trapped Rossby waves. (For overviews, see Matsuno (1966), Holton (2004, pp. 394–400) or Andrews et al. (1987, pp. 200–208).) The Kelvin wave exhibits pressure perturbations peaking at the equator, with strong zonally divergent east-west winds; these waves propagate to the east. The east-west winds in the Kelvin wave cause strong north-south Coriolis forces that prevent the expansion of the pressure perturbations in latitude; however, nothing resists the pressure perturbations in longitude, and so the Kelvin wave propagates zonally like a gravity wave at a speed  $\sqrt{gH}$ . In contrast, the Rossby wave exhibits pressure perturbations that peak off the equator and vortical winds that encircle these pressure perturbations; these waves propagate to the west. See Holton (2004, Figure 11.15) and Matsuno (1966, Figure 4(c)), respectively, for visuals of these two wave types.

The link between our solutions and wave dynamics becomes even tighter when one compares the detailed spatial structure of the solutions to these tropical wave modes. Building on a long history of work in tropical dynamics (e.g., Matsuno 1966; Gill 1980), Showman & Polvani (2011) showed that the behavior of steady, forced, damped solutions like those in Figures 3 and 4 can be interpreted in terms of standing, planetary-scale Rossby and Kelvin waves. Examining, for example, the  $\tau_{\text{rad}} = 1$  day,  $\tau_{\text{drag}} = 1$  day models in Figure 4, the off-equatorial behavior, including the off-equatorial pressure maxima and the vortical winds that encircle them (clockwise in northern hemisphere, counterclockwise in southern hemisphere), is dynamically analogous to the equatorially trapped Rossby wave mentioned above. The low-latitude behavior, with winds that zonally diverge from a point east of the substellar point, is dynamically analogous

the height by  $\Delta h$ . This timescale is simply given by

$$\tau \sim \frac{\Delta h}{H\nabla \cdot \mathbf{v}} \sim \frac{\Delta h L}{HU}, \quad (31)$$

where  $U$  is the wind speed associated with the wave motion. In the absence of forcing or damping, the horizontal momentum equation is the linearized version of Equation (1) with the right-hand side set to zero. In the absence of rotational effects, the balance is simply between the time-derivative term and the pressure-gradient term, which to order of magnitude is

$$\frac{U}{\tau} \sim g \frac{\Delta h}{L}. \quad (32)$$

Combining these two equations immediately yields  $\tau \sim \frac{L}{\sqrt{gH}}$ .

<sup>10</sup> This relationship can also be obtained by equating the rate of vertical mass transport  $\sim \rho_{\text{upper}} \Delta h L^2 / \tau_{\text{vert}}$  to the rate of horizontal mass transport  $\sim \rho_{\text{upper}} H L^2 / \tau_{\text{adv}}$ .

<sup>11</sup> Specifically, consider for simplicity a one-dimensional, non-rotating linear shallow-water system in the absence of forcing or damping. If a local region begins with a height  $\Delta h$  different from its surrounding regions, the timescale for the wave to propagate over its wavelength  $L$  will be determined by the time needed for horizontal convergence/divergence to locally change

to the equatorial Kelvin wave mentioned above. See Gill (1980) and Showman & Polvani (2011) for further discussion. Again, here is the key point: the physical mechanisms that cause stretching/contraction of the shallow-water column and wave propagation of Kelvin and Rossby waves in the free, time-dependent case are *the same physical mechanisms* that regulate the spatial variations of the thickness in our forced, damped, steady solutions.

In sum, if the radiative and frictional damping times are sufficiently long, the Kelvin and Rossby waves act efficiently to flatten the layer, and the day-night thickness differences are small. If the radiative and frictional damping times are sufficiently short, the Kelvin and Rossby waves are damped and cannot propagate zonally; the thermal structure is then close to radiative equilibrium. Although our solutions are steady, this similarity to wave dynamics explains the natural emergence of a wave timescale in controlling the transition between small and large day-night contrast. In particular, because the Kelvin wave propagates at a speed  $\sqrt{gH}$ , the fundamental wave timescale that emerges is  $L/\sqrt{gH}$ .

It is important to emphasize that, despite the importance of wave timescales, horizontal advection nevertheless plays a crucial role in the dynamics. Consider an imaginary surface at the terminator dividing the planet into dayside and nightside hemispheres. It is horizontal advection across this surface that ultimately transports heat from day to night, thereby allowing each hemisphere to reach a steady state in the presence of continual dayside heating and nightside cooling. In the linear limit of our shallow-water model, this transport manifests as advection of the mean thickness (i.e.,  $uH$  integrated around the terminator), although advection of thickness *variations* can also play a role at high amplitude, when these variations are not small relative to  $H$ . The importance of horizontal advection does not mean that the flow behavior is controlled by the horizontal advection timescale, and indeed we have shown that it is generally not, particularly when the forcing amplitude is weak.

## 6. APPLICATION TO HOT JUPITER OBSERVATIONS

Here we compare predictions for the day-night height difference,  $A$ , obtained from our shallow water model to the observed fractional infrared flux variations,  $A_{\text{obs}}$ , on hot Jupiters. Because the shallow water equations do not explicitly include stellar irradiation, we have to express our model's input parameters  $\tau_{\text{rad}}$  and  $\tau_{\text{drag}}$  in terms of  $T_{\text{eq}}$  (our proxy for stellar irradiation). We find the dependence of the radiative timescale on  $T_{\text{eq}}$  by approximating  $\tau_{\text{rad}}$  as the ratio between the available thermal energy per unit area within a pressure scale-height and the net radiative flux from that layer (Showman & Guillot 2002),

$$\tau_{\text{rad}} \sim \frac{P c_p}{4g\sigma T_{\text{eq}}^3}, \quad (33)$$

where  $P$  is the atmospheric pressure at the emitting layer,  $c_p$  is the specific heat, and  $\sigma$  is the Stefan-Boltzmann constant. We have chosen to leave  $\tau_{\text{drag}}$  as a free parameter, because the source of atmospheric drag in gas giants remains largely unknown (e.g., Perna et al. 2010; Li & Goodman 2010; Showman et al. 2010), and because our results suggest a weak dependence of  $A$  on  $\tau_{\text{drag}}$  (see Figure 6(a)).<sup>12</sup>

<sup>12</sup> In the case of hot Jupiters, the main candidate for atmospheric drag is

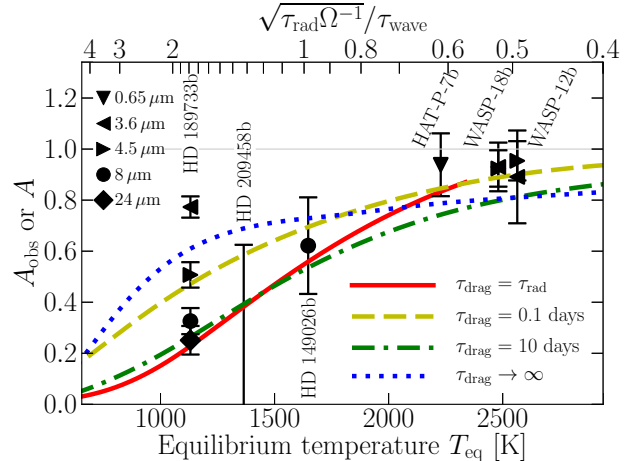


FIG. 11.— Same as Figure 1, but including shallow water model results. Black symbols are fractional day-night flux variations ( $A_{\text{obs}}$ ) for hot Jupiters with measured light curves, as explained in detail in Figure 1. Colored dashed curves show model results for the normalized day-night height difference  $A$  for constant  $\tau_{\text{drag}}$ , expressed in Earth days, while the solid red line shows the solution when  $\tau_{\text{drag}} = \tau_{\text{rad}}$ . Equilibrium temperatures ( $T_{\text{eq}}$ ) for the model were estimated with equation (33) with  $c_p = 10^4 \text{ J kg}^{-1} \text{ K}^{-1}$ ,  $g = 10 \text{ m s}^{-2}$ , and  $P = 0.25 \text{ bar}$ , which is approximately the pressure of the layer radiating to space (compare upper and lower  $x$ -axes). Because plotted solutions are (mostly) in the weak-drag regime, all curves lie close together and broadly reproduce the observational trend of increasing  $A_{\text{obs}}$  with increasing  $T_{\text{eq}}$ .

We plot model values for  $A$  together with  $A_{\text{obs}}$  from hot Jupiter observations in Figure 11. Each broken curve shows model results for  $A$  for a constant value of  $\tau_{\text{drag}}$ , ranging from values that are marginally in the strong drag regime ( $\tau_{\text{drag}} = 0.1 \text{ days}$ ) to no drag ( $\tau_{\text{drag}} \rightarrow \infty$ ). Additionally, we show the solution when  $\tau_{\text{drag}} = \tau_{\text{rad}}$  with the solid red line. Because  $\tau_{\text{drag}}$  is fixed, the only remaining free variable is  $\tau_{\text{rad}}$ , which we express in terms of  $T_{\text{eq}}$  using equation (33) (compare upper and lower  $x$ -axes). All curves follow roughly the same path which reproduces the observational trend of increasing  $A$  with equilibrium temperature  $T_{\text{eq}}$ . The curves run close to each other because the models considered are either in the weak drag regime or barely in the strong drag regime. Solutions with  $\tau_{\text{drag}} < 0.1 \text{ days}$  are numerically challenging and were therefore not explored. In any case, for the case of magnetic drag, the temperatures required to reach such low drag timescales are  $\geq 1500 \text{ K}$  (Perna et al. 2010), where the corresponding  $\tau_{\text{rad}}$  is already so low that  $A \sim 1$  regardless of the strength of drag. In summary, when  $\sqrt{\tau_{\text{rad}}/\Omega}$  is shorter than  $\tau_{\text{wave}}$ , the Kelvin and Rossby waves that emerge near the equator are damped before they can propagate zonally, resulting in  $A \sim 1$ . In contrast, when  $\sqrt{\tau_{\text{rad}}/\Omega}$  is long compared to  $\tau_{\text{wave}}$ , the emerging waves can propagate far enough to flatten the fluid layer, resulting in  $A \sim 0$ .

## 7. CONCLUSIONS

We have presented a simple atmospheric model for tidally locked exoplanets that reproduces the observed transition

Lorentz-force breaking of the thermally ionized atmosphere. For the case of HD 209458b, Perna et al. (2010) estimate that  $\tau_{\text{drag}}$  could reach values as low as  $\sim 0.1 \text{ days}$  on the planet's dayside, which matches our lowest considered  $\tau_{\text{drag}}$ . Rauscher & Menou (2013) found that the inclusion of Lorentz drag in their global circulation model of HD 209458b changes the ratio between maximum and minimum flux emission from the planet by up to 5% when compared to a drag-free model (see their Table 2). Although their study excluded the most strongly irradiated hot Jupiters, their simulations are in accordance with our result that  $A$  depends only weakly on  $\tau_{\text{drag}}$ .

from atmospheres with longitudinally uniform temperatures to atmospheres with large day-night temperature gradients as stellar insolation increases (Figure 11). In our model we have parameterized the stellar insolation in terms of a radiative timescale,  $\tau_{\text{rad}}$ , and frictional processes in terms of a drag timescale,  $\tau_{\text{drag}}$ . The shallow water model contains two additional natural timescales: the rotation period of the planet ( $\sim\Omega^{-1}$ ), and  $\tau_{\text{wave}}$ , the timescale over which gravity waves travel horizontally over planetary distances. We have developed an analytical scaling theory to estimate the heat redistribution efficiency in terms of these four timescales. Our scaling theory predicts that for sufficiently weak atmospheric drag, the temperature distribution on the planet can be estimated by the ratio of  $\tau_{\text{wave}}$  and  $\sqrt{\tau_{\text{rad}}/\Omega}$ . Drag will influence the day-night temperature contrast if it operates on a timescale shorter than  $\Omega^{-1}$ . In this drag-dominated regime, the heat redistribution efficiency will depend on the ratio of  $\tau_{\text{wave}}$  and  $\sqrt{\tau_{\text{rad}}\tau_{\text{drag}}}$ . These scaling relations are summarized in equation (24). We provide two physical interpretations to understand why these timescales arise from the shallow water model. We derive the first interpretation by noting that the same physical mechanisms that generate equatorially trapped waves in an undamped shallow water model also regulate the steady-state solutions of our forced-damped model. The heat redistribution efficiency is therefore related to the characteristic distance that waves can travel before they are damped. This distance is set by the relative magnitudes of the timescale for waves to travel over planetary distances,  $\tau_{\text{wave}}$ , and the timescale for the waves to damp.

For the second interpretation, we recognize that the timescale comparisons of equation (24) can be written as  $\tau_{\text{rad}} \sim \tau_{\text{vert}}$ , where  $\tau_{\text{vert}}$  is the timescale for a parcel to advect vertically over a distance equal to the day-night differ-

ence in thickness. This criterion emerges from the fact that, as long as forcing amplitudes are not large, it is primarily vertical advection—and not horizontal advection, as commonly assumed—that balances radiative relaxation in the continuity equation. Despite this fact, the timescale comparison between  $\tau_{\text{rad}}$  and the horizontal advection timescale,  $\tau_{\text{adv}}$ , provides reasonable estimates for the heat redistribution efficiency on hot Jupiters. This is because these gas giants have strongly forced atmospheres ( $\Delta h_{\text{eq}}/H \sim 1$ ), where  $\tau_{\text{adv}}$  becomes comparable to  $\tau_{\text{vert}}$  (see equation (30)), and where horizontal and vertical thermal advectons become comparable. In weakly forced systems, the timescale comparison between  $\tau_{\text{rad}}$  and  $\tau_{\text{adv}}$  is a poor predictor for the heat redistribution efficiency, as we show in Figure 10. In contrast, the timescale comparison between  $\tau_{\text{rad}}$  vs.  $\tau_{\text{vert}}$ —derived from the dynamical equations—yields a more accurate estimate of the heat redistribution efficiency at any  $\Delta h_{\text{eq}}/H$ , including the strongly forced hot Jupiters.

We are extremely thankful to Eugene Chiang, whose extensive comments and manuscript revisions greatly helped to clarify the presentation of this work. This project was initiated at the International Summer Institute for Modeling in Astrophysics (ISIMA) at the Kavli Institute for Astronomy and Astrophysics (KIAA) at Peking University. We thank Pascale Garaud and Doug Lin for their help in organizing the program. We are also grateful to an anonymous referee for promoting a more thorough discussion on the limitations of our model. This work was supported by NASA Origins grants NNX08AF27G and NNX12AI79G to A.P.S., and by graduate fellowships from the National Science Foundation and UC MEXUS/CONACyT awarded to D.P.-B.

## REFERENCES

- Andrews, D., Holton, J., & Leovy, C. 1987, *Middle Atmosphere Dynamics* (Academic Press, New York)
- Borucki, W. J., et al. 2009, *Science*, 325, 709
- Bretherton, C. S., & Smolarkiewicz, P. K. 1989, *Journal of Atmospheric Sciences*, 46, 740
- Bretherton, C. S., & Sobel, A. H. 2003, *Journal of Atmospheric Sciences*, 60, 451
- Cho, J. Y.-K., Menou, K., Hansen, B. M. S., & Seager, S. 2003, *ApJ*, 587, L117
- . 2008, *Astrophys. J.*, 675, 817
- Cho, J. Y.-K., & Polvani, L. M. 1996, *Physics of Fluids*, 8, 1531
- Cooper, C. S., & Showman, A. P. 2005, *ApJ*, 629, L45
- Cowan, N. B., & Agol, E. 2011, *Astrophys. J.*, 729, 54
- Cowan, N. B., Agol, E., & Charbonneau, D. 2007, *Mon. Not. Roy. Astron. Soc.*, 379, 641
- Cowan, N. B., Machalek, P., Croll, B., Shekhtman, L. M., Burrows, A., Deming, D., Greene, T., & Hora, J. L. 2012, *Astrophys. J.*, 747, 82
- Crossfield, I. J. M., Hansen, B. M. S., Harrington, J., Cho, J. Y.-K., Deming, D., Menou, K., & Seager, S. 2010, *Astrophys. J.*, 723, 1436
- Deming, D., & Seager, S. 2009, *Nature*, 462, 301
- Dowling, T. E., & Ingersoll, A. P. 1989, *Journal of Atmospheric Sciences*, 46, 3256
- Fortney, J. J., Lodders, K., Marley, M. S., & Freedman, R. S. 2008, *Astrophys. J.*, 678, 1419
- Gill, A. E. 1980, *Quarterly Journal of the Royal Meteorological Society*, 106, 447
- Gill, A. E. 1982, *Atmosphere-Ocean Dynamics* (Academic Press, New York)
- Guillot, T., Burrows, A., Hubbard, W. B., Lunine, J. I., & Saumon, D. 1996, *ApJ*, 459, L35
- Hack, J. J., & Jakob, R. 1992, Tech. rep., National Center for Atmospheric Research Technical note NCAR/TN-343+STR, Boulder, CO
- Harrington, J., Hansen, B. M., Luszcz, S. H., Seager, S., Deming, D., Menou, K., Cho, J. Y.-K., & Richardson, L. J. 2006, *Science*, 314, 623
- Heng, K., Menou, K., & Phillipps, P. J. 2011, *Mon. Not. Roy. Astron. Soc.*, 413, 2380
- Holton, J. 2004, *An Introduction to Dynamic Meteorology*, 4th Ed. (Academic Press, San Diego)
- Johnson, R. S. 1997, *A Modern Introduction to the Mathematical Theory of Water Waves* (Cambridge University Press, Cambridge, UK)
- Knutson, H. 2011, AGU Fall Meeting Abstracts, C4
- Knutson, H. A., Charbonneau, D., Cowan, N. B., Fortney, J. J., Showman, A. P., Agol, E., & Henry, G. W. 2009a, *Astrophys. J.*, 703, 769
- Knutson, H. A., et al. 2007, *Nature*, 447, 183
- . 2009b, *Astrophys. J.*, 690, 822
- . 2012, *Astrophys. J.*, 754, 22
- Laughlin, G., Deming, D., Langton, J., Kasen, D., Vogt, S., Butler, P., Rivera, E., & Meschiari, S. 2009, *Nature*, 457, 562
- Lewis, N. K., et al. 2013, *Astrophys. J.*, 766, 95
- Li, J., & Goodman, J. 2010, *Astrophys. J.*, 725, 1146
- Liu, B., & Showman, A. P. 2013, *Astrophys. J.*, 770, 42
- Lovis, C., & Fischer, D. 2010, *Exoplanets* (ed. S. Seager, University of Arizona Press, Tucson)
- Matsuno, T. 1966, *J. Meteorol. Soc. Japan*, 44, 25
- Maxted, P. F. L., et al. 2013, *Mon. Not. Roy. Astron. Soc.*, 428, 2645
- Menou, K., Cho, J. Y.-K., Seager, S., & Hansen, B. M. S. 2003, *ApJ*, 587, L113
- Perna, R., Heng, K., & Pont, F. 2012, *Astrophys. J.*, 751, 59
- Perna, R., Menou, K., & Rauscher, E. 2010, *Astrophys. J.*, 719, 1421
- Rauscher, E., & Menou, K. 2010, *Astrophys. J.*, 714, 1334
- . 2013, *Astrophys. J.*, 764, 103
- Scott, R. K., & Polvani, L. M. 2007, *Journal of Atmospheric Sciences*, 64, 3158
- Shell, K. M., & Held, I. M. 2004, *Journal of Atmospheric Sciences*, 61, 2928
- Showman, A. P. 2007, *Journal of Atmospheric Sciences*, 64, 3132
- Showman, A. P., Cho, J. Y.-K., & Menou, K. 2010, *Exoplanets* (ed. S. Seager, University of Arizona Press, Tucson)



- Showman, A. P., Cooper, C. S., Fortney, J. J., & Marley, M. S. 2008, *Astrophys. J.*, 682, 559
- Showman, A. P., Fortney, J. J., Lewis, N. K., & Shabram, M. 2013a, *Astrophys. J.*, 762, 24
- Showman, A. P., & Guillot, T. 2002, *Astron. Astrophys.*, 385, 166
- Showman, A. P., & Polvani, L. M. 2010, *Geophys. Res. Lett.*, 37, 18811
- . 2011, *Astrophys. J.*, 738, 71
- Showman, A. P., Wordsworth, R. D., Merlis, T. M., & Kaspi, Y. 2013b, *ArXiv e-prints*
- Sobel, A. H. 2002, *Chaos*, 12, 451
- Sobel, A. H., Nilsson, J., & Polvani, L. M. 2001, *Journal of Atmospheric Sciences*, 58, 3650
- Vallis, G. K. 2006, *Atmospheric and Oceanic Fluid Dynamics* (Cambridge University Press, Cambridge)